Gondwana Research 33 (2016) 24–43

Contents lists available at ScienceDirect

Gondwana Research

journal homepage: www.elsevier.com/locate/gr

GR Focus Review

Seismic anisotropy tomography: New insight into subduction dynamics

Dapeng Zhao [a], Sheng Yu [b], Xin Liu [a]

[a] Department of Geophysics, Tohoku University, Sendai 980-8578, Japan
[b] Department of Earth Sciences, National Natural Science Foundation of China, Beijing 100085, China

ARTICLE INFO

Article history:
Received 14 February 2015
Received in revised form 27 May 2015
Accepted 28 May 2015
Available online 6 June 2015

Keywords:
Seismic tomography
Azimuthal anisotropy
Radial anisotropy
Earthquakes
Subduction zones
Mantle wedge
Subducting slabs
Mantle dynamics

ABSTRACT

Body-wave and surface-wave tomography, receiver-function imaging, and shear-wave splitting measurements have shown that seismic anisotropy and heterogeneity coexist in all parts of subduction zones, providing important constraints on the mantle flow and subduction dynamics. P-wave anisotropy tomography is a new but powerful tool for mapping three-dimensional variations of azimuthal and radial seismic anisotropy in the crust and mantle. P-wave azimuthal-anisotropy tomography has been applied widely to the Circum-Pacific subduction zones, Mainland China and North America, whereas P-wave radial-anisotropy tomography was applied to only a few areas including Northeast Japan, Southwest Japan and North China Craton. These studies have revealed complex anisotropy in the crust and mantle lithosphere associated with the surface geology and tectonics, anisotropy reflecting subduction-driven corner flow in the mantle wedge, frozen-in fossil anisotropy in the subducting slabs formed at the mid-ocean ridge, as well as olivine fabric transitions due to changes in water content, stress and temperature. Shear-wave splitting tomography methods have been also proposed, but their applications are still limited and preliminary. There is a discrepancy between the surface-wave and body-wave tomographic models in radial anisotropy of the mantle wedge beneath Japan, which is a puzzle but an intriguing topic for future studies.

Contents

1. Introduction

During the past three decades, a great number of seismological studies have revealed that seismic velocity and attenuation heterogeneity, as well as seismic anisotropy, exist widely in the Earth's interior. The

E-mail address: dapeng.zhao.d2@tohoku.ac.jp (D. Zhao).

http://dx.doi.org/10.1016/j.gr.2015.05.008

structural heterogeneities in the crust and mantle have been mapped by using seismic tomography and receiver-function methods, whereas seismic anisotropy has been detected by shear-wave splitting (SWS) measurements, apparent discrepancy between Love and Rayleigh waves, and azimuthal variations of Pn-wave velocity (e.g., Zhao, 2012; Long, 2013; Zhao, 2015a for recent reviews). However, in the conventional tomographic studies, in particular, body-wave tomography, the Earth is usually assumed to be isotropic to the propagation of seismic waves. As pointed out by Anderson (1989), this assumption is made for mathematical convenience, and the fact that a large body of seismic data can be satisfactorily modeled with this assumption does not prove that the Earth is isotropic. Seismic anisotropy can cause the largest variations in seismic velocity, which can be even greater than those caused by changes in temperature, composition or mineralogy. Hence, anisotropy is a first-order effect (Anderson, 1989).

Seismic anisotropy is a very useful and important physical parameter, because it can provide a wealth of new information regarding dynamic processes in the crust and mantle (e.g., Cara, 2002; Fouch and Rondenay, 2006; Wang and Zhao, 2008; Long, 2013; Wang and Zhao, 2013; Koulakov et al., 2015). The major causes of seismic anisotropy are lattice-preferred orientation (LPO) and shape-preferred orientation (SPO) of the materials constituting the Earth. In the crust, orientations of local and regional structure and tectonics can cause seismic anisotropy, such as fault systems (e.g., Zhang and Schwartz, 1994; Bokelmann, 1995; Huang and Zhao, 2013; Huang et al., 2014; Koulakov et al., 2015). In the mantle, seismic anisotropy may reflect convection flows and is usually interpreted by LPO of olivine crystals (e.g., Karato and Wu, 1993; Fouch and Rondenay, 2006; Wang and Zhao, 2008; Long, 2013; Wang and Zhao, 2013). However, the relationship between anisotropy and mantle flows is uncertain in some cases, e.g., when abundant fluids and melts exist, the anisotropy may be orthogonal to the flow direction. The petrologic basis of such behaviors has been investigated in laboratory experiments (e.g., Jung and Karato, 2001; Karato et al., 2008).

Both body-wave and surface-wave data can be used to study seismic anisotropy. The body-wave methods include SWS, receiver functions, and P-wave travel-time inversion. Fouch and Rondenay (2006) made a detailed review of the methods for studying seismic anisotropy, as well as their advantages and limitations. In the past three decades, many researchers have attempted to use P-wave travel-time data to study anisotropy tomography (e.g., Babuska et al., 1984; Hearn, 1984; Hirahara and Ishikawa, 1984; Hirahara, 1988; Babuska and Cara, 1991; Mochizuki, 1995; Gresillaud and Cara, 1996; Hearn, 1996; Plomerova et al., 1996; Mochizuki, 1997; Lees and Wu, 1999; Wu and Lees, 1999; Bokelmann, 2002; Eberhart-Phillips and Henderson, 2004; Ishise and Oda, 2005, 2008; Wang and Zhao, 2008; Koulakov et al., 2009; Eken et al., 2010; Plomerova et al., 2011; Tian and Zhao, 2012a; Huang and Zhao, 2013; Wang and Zhao, 2013; Wei et al., 2013; Koulakov et al., 2015; Menke, 2015; Wei et al., 2015). However, reliable and geologically reasonable results have been obtained only in recent years, thanks to the availability of abundant high-quality arrival-time data recorded by dense seismic arrays of permanent and portable stations at local and regional scales. The Pn-wave tomography can only estimate two-dimensional (2-D) P-wave velocity (Vp) variations and azimuthal anisotropy in the uppermost mantle directly beneath the Moho discontinuity (e.g., Hearn, 1996), whereas P-wave anisotropy tomography can determine three-dimensional (3-D) distribution of Vp anisotropy in the crust and mantle beneath a seismic network.

Measuring SWS is a popular and useful method for studying (detecting) seismic anisotropy. A great number of researchers have used this method to study seismic anisotropy in many regions of the world, which have provided important information on mantle dynamics (e.g., Crampin, 1984; Silver, 1996; Savage, 1999; Huang et al., 2011a,b; Long, 2013). However, the SWS measurements have a poor depth resolution, and so their interpretations are usually not unique. This drawback can be overcome by Vp anisotropy tomography.

Many researchers have used surface-wave tomography to study seismic heterogeneity and anisotropy (e.g., Tanimoto and Anderson, 1984; Nishimura and Forsyth, 1988; Montagner and Tanimoto, 1991; Ritzwoller and Lavely, 1995; Nettles and Dziewonski, 2008; Yoshizawa et al., 2010; Montagner, 2011; Yuan et al., 2011). As compared with body-wave tomography, however, surface-wave tomography generally has a lower spatial resolution, and so it has been mainly applied to study shear-wave velocity (Vs) structure and anisotropy in the crust and upper mantle at a global scale or a large regional scale for oceanic or continental regions. The information on subduction dynamics provided by surface-wave tomography has been limited by its lower spatial resolution. Recently, Long (2013) made a detailed review of seismic anisotropy studies of subduction zones, whereas her review focused on the SWS measurements and receiver function studies.

In this article, we review the methods and applications of body-wave anisotropy tomography and discuss their implications for the structure and dynamics of subduction zones. Some related SWS measurements and high-resolution surface-wave tomography studies are also mentioned for better interpreting the results of body-wave anisotropy tomography.

2. P-wave anisotropy tomography: Methods

Twenty one independent elastic moduli are required to fully express an anisotropic medium, which is very hard to handle in both theory and practice. Fortunately, anisotropy with hexagonal symmetry is a proper approximation to the materials in the Earth's crust and mantle, which can reduce the number of physical parameters describing seismic anisotropy (e.g., Christensen, 1984; Park and Yu, 1993; Maupin and Park, 2007). To further simplify the problem, we can assume the hexagonal symmetry to be horizontal when the azimuthal anisotropy is concerned in SWS measurements (e.g., Crampin, 1984; Silver, 1996; Savage, 1999; Huang et al., 2011a,b; Long, 2013) and P-wave velocity studies (e.g., Hess, 1964; Backus, 1965; Raitt et al., 1969; Hearn, 1996; Eberhart-Phillips and Henderson, 2004; Wang and Zhao, 2008, 2013); whereas we can assume the hexagonal symmetry to be vertical when the radial anisotropy is concerned in the form of a Vsh/Vsv variation (Vsh and Vsv are the velocities of shear waves polarized horizontally and vertically, respectively) in surface-wave studies (e.g., Nettles and Dziewonski, 2008; Fichtner et al., 2010; Yuan et al., 2011) and in the form of a Vph/Vpv variation (Vph and Vpv are the velocities of P-waves propagating horizontally and vertically, respectively) in P-wave velocity studies (e.g., Ishise et al., 2012; Wang and Zhao, 2013; Wang et al., 2014). Here we introduce the recent tomographic methods for P-wave azimuthal and radial anisotropy, following Wang and Zhao (2008, 2013).

2.1. Azimuthal anisotropy tomography

For hexagonal anisotropy, P-wave slowness can be expressed as (Barclay et al., 1998):

$$S = S_0 + M\cos(2\theta), \tag{1}$$

where S is the total slowness (i.e., 1/V), S_0 is the average slowness (i.e., isotropic component), θ is the angle between the propagation vector and the symmetry axis (Fig. 1), and M is the parameter for anisotropy. In a weak anisotropic medium with a horizontal hexagonal symmetry axis (Fig. 1a), the P-wave slowness of a horizontal ray can be approximately expressed as (e.g., Backus, 1965; Raitt et al., 1969; Hearn, 1996; Eberhart-Phillips and Henderson, 2004; Wang and Zhao, 2008, 2013):

$$S(\phi) = S_0(1 + A_1\cos(2\phi) + B_1\sin(2\phi)), \tag{2}$$

where S is the total slowness, S_0 is the azimuthal average slowness, A_1 and B_1 are the azimuthal anisotropy parameters, and ϕ is the ray path

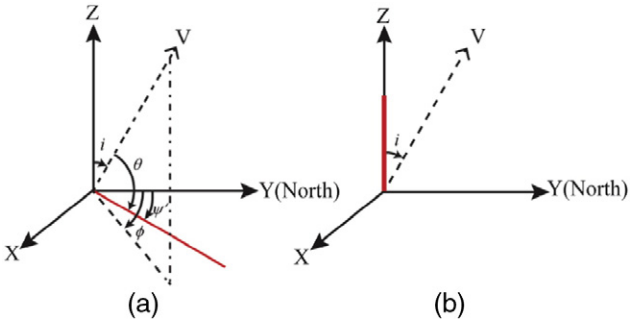

Fig. 1. The coordinate system specifying a ray path (the dashed line) and the hexagonal symmetry axis (the red line) for (a) azimuthal anisotropy and (b) radial anisotropy (Ishise et al., 2012; Wang and Zhao, 2013). V is the propagation vector of a ray with incident angle i and azimuthal angle ϕ. θ is the angle between the propagation vector and the symmetry axis. For the azimuthal anisotropy (a), the azimuthal angle ψ' of the hexagonal symmetry axis is normal to the fast-velocity direction.

azimuth. Then the fast-velocity direction (FVD) ψ and the amplitude α of the azimuthal anisotropy are expressed as follows:

$$\psi = \begin{cases} \frac{1}{2}\tan^{-1}\left(\frac{B_1}{A_1}\right) + \begin{cases} \frac{\pi}{2}, & A_1>0 \\ 0, & A_1<0, \end{cases} \\ -\frac{\pi}{4}, A_1 = 0, B_1>0, \\ \frac{\pi}{4}, A_1 = 0, B_1<0, \end{cases}$$
$$\alpha = \frac{V_f - V_s}{2V_0} = \frac{\sqrt{A_1^2 + B_1^2}}{1-\left(A_1^2 + B_1^2\right)}, \tag{3}$$

where V_0 is the average isotropic velocity; V_f and V_s are the velocities in the fast and slow directions, respectively. For a dipping ray, a similar relation as Eq. (2) can be obtained by correcting for the effect of the ray dipping angle using the following relation between θ and the propagation vector (Eberhart-Phillips and Henderson, 2004):

$$\cos\theta = \sin i(\sin\phi\sin\psi + \cos\phi\cos\psi), \tag{4}$$

where i is the incident angle of a ray path. Thus, for local earthquakes which are located in the modeling space, we have the following observation equation:

$$T_{mn}^{obs} - T_{mn}^{cal} = \left(\frac{\partial T}{\partial\varphi}\right)_{mn}\Delta\varphi_n + \left(\frac{\partial T}{\partial\lambda}\right)_{mn}\Delta\lambda_n + \left(\frac{\partial T}{\partial h}\right)_{mn}\Delta h_n + \Delta T_{0n} + \sum_p\left(\frac{\partial T}{\partial V_p}\Delta V_p\right) + \sum_q\left(\frac{\partial T}{\partial A_{1q}}\Delta A_{1q} + \frac{\partial T}{\partial B_{1q}}\Delta B_{1q}\right) + E_{mn}, \tag{5}$$

where T_{mn}^{obs} and T_{mn}^{cal} are the observed and calculated travel times from the nth event to the mth station, φ_n, λ_n, h_n and T_{0n} are the latitude, longitude, focal depth and origin time of the nth event, respectively, and Δ denotes the perturbation of a parameter. Two 3-D grid nets are set up in the modeling volume, one finer grid is for expressing the 3-D isotropic velocity structure, whereas the other coarser grid is for expressing the 3-D anisotropic structure (Huang et al., 2011c; Wang and Zhao, 2013). In Eq. (5), V_p is the isotropic velocity at the pth node of the finer grid, whereas A_{1q} and B_{1q} are the azimuthal anisotropy parameters at the qth node of the coarser grid. E_{mn} represents higher-order terms of perturbations and data error. The first four terms on the right-hand side of Eq. (5) represent contributions of the four hypocentral parameters, which can be obtained using the formulas of Engdahl and Lee (1976).

2.2. Radial anisotropy tomography

If the hexagonal symmetry axis is vertical (Fig. 1b), Eq. (1) can be rewritten as follows (Ishise et al., 2012; Wang and Zhao, 2013):

$$S = S_0 + M\cos(2i) = S_0\left(1 + \frac{M}{S_0}\cos(2i)\right) = S_0(1 + M_1\cos(2i)). \tag{6}$$

The amplitude β of radial anisotropy is defined as:

$$\beta = \frac{V_{ph} - V_{pv}}{2V_0} = \frac{M_1}{1-M_1^2}, \tag{7}$$

Hence, $\beta > 0$ indicates that the horizontally-propagating P-wave travels faster than the vertical one, i.e., $V_{ph} > V_{pv}$.

By using Eq. (6), the travel time T_k of the kth ray segment with length d can be written as:

$$T_k = dS = d(1 + M_{1k}\cos(2i_k))/V_k,$$
$$T = \sum_k T_k, \tag{8}$$

where T is the total travel time of the ray, V_k is the isotropic velocity at the middle point of the kth ray segment, M_{1k} is the parameter for the radial anisotropy at the middle point of the kth ray segment, and i_k is the incident angle of the kth ray segment. Thus, the partial derivatives of the travel time with respect to the velocity and radial anisotropy are expressed as:

$$\frac{\partial T}{\partial V_k} = -d(1 + M_{1k}\cos(2i_k))/V_k^2,$$
$$\frac{\partial T}{\partial M_{1k}} = \frac{d}{V_k}\cos(2i_k). \tag{9}$$

Similar to the isotropic tomography (Zhao et al., 1992) and Vp azimuthal anisotropy tomography (Wang and Zhao, 2008), V_k and M_{1k} at a point are calculated using linear interpolation of the parameters at the eight grid nodes surrounding that point. Then, the travel-time residual can be written as:

$$T_{mn}^{obs} - T_{mn}^{cal} = \left(\frac{\partial T}{\partial\varphi}\right)_{mn}\Delta\varphi_n + \left(\frac{\partial T}{\partial\lambda}\right)_{mn}\Delta\lambda_n + \left(\frac{\partial T}{\partial h}\right)_{mn}\Delta h_n + \Delta T_{0n} + \sum_p\left(\frac{\partial T}{\partial V_p}\Delta V_p\right) + \sum_q\left(\frac{\partial T}{\partial M_{1q}}\Delta M_{1q}\right) + E_{mn}. \tag{10}$$

Similar to the case of isotropic velocity tomography (Zhao et al., 1992, 1994), Eqs. (5) and (10) are solved using the LSQR algorithm with damping and smoothing regularizations (Wang and Zhao, 2008, 2013; Zhao, 2015a).

In the above-mentioned methods, the symmetry axis of seismic anisotropy is assumed to be either horizontal or vertical. In the Earth's crust and mantle, however, the symmetry axis could be inclined, such as within the subducting slab and the corner flow in the mantle wedge. Some studies have focused on such an issue (e.g., Plomerova et al., 1996, 2011).

3. P-wave anisotropy tomography: Applications

As compared with isotropic tomography, azimuthal anisotropy tomography requires better coverage of ray paths in different directions, and radial anisotropy tomography requires rays travelling in both horizontal and vertical directions in the study volume. This is a challenge to most applications of P-wave anisotropy tomography. Fortunately, in some regions such as the Japan subduction zone, dense seismic networks have been installed for a long period recording the abundant seismicity in both the crust and the subducting slabs (Zhao, 2012, 2015a,b), which provide excellent ray path coverage in the crust and upper

mantle, enabling us to determine a high-resolution P-wave anisotropy tomography. In other less instrumented regions, intriguing results have been also obtained in recent years, though with a lower resolution.

3.1. Northeast Japan

The Northeast Japan arc is characterized by the subduction of the Pacific plate beneath the Okhotsk (or North American) plate, forming a typical subduction zone (Fig. 2). During the past three decades many tomographic studies have been made to investigate the 3-D P and S wave velocity and attenuation structures of the crust and upper mantle (e.g., Hasemi et al., 1984; Umino and Hasegawa, 1984; Zhao et al., 1992; Tsumura et al., 2000; Mishra et al., 2003; Wang and Zhao, 2006; Xia et al., 2008; Zhao et al., 2011a,b; Tong et al., 2012; Abdelwahed and Zhao, 2014; Liu et al., 2014). The deeper structure of the subducting Pacific slab and the mantle below the slab has been investigated using teleseismic tomography (Zhao et al., 1994; Abdelwahed and Zhao, 2007; Zhao et al., 2012). These studies clearly revealed the high-velocity (high-V) and low-attenuation (high-Q) subducting Pacific slab and arc magma-related low-velocity (low-V) and high-attenuation (low-Q) anomalies in the crust and upper-mantle wedge beneath the volcanic front and back-arc areas. SWS measurements have been made to study the anisotropic structure of the subduction zone (e.g., Okada et al., 1995; Nakajima et al., 2006; Huang et al., 2011a,b; Watanabe and Oda, 2014). The results show that trench-parallel S-wave anisotropy appears in the forearc area, whereas trench-normal anisotropy exists in the back-arc area.

In the past decade, P-wave anisotropy tomography has been used to map the 3-D anisotropic structure beneath NE Japan. Ishise and Oda (2005) used ~15,000 P-wave arrival-time data of 961 local shallow and intermediate-depth earthquakes recorded by 47 seismic stations to determine P-wave anisotropy tomography beneath Tohoku. Their results show that the FVD is in mostly E-W direction in the upper crust, nearly N-S and E-W directions in the lower crust, E-W direction in the mantle wedge, and N-S direction in the descending Pacific slab. These features of the Vp anisotropy structure are generally consistent with those of the SWS measurements. The plausible cause of the crustal anisotropy may be alignment or preferred orientation of micro-cracks and crustal minerals. The mantle wedge anisotropy is attributed to LPO of mantle minerals arising from the current mantle processes such as the mantle-wedge convection and the plate motion. The FVD in the slab is north-south (Fig. 2), almost perpendicular to the magnetic lineation of the oceanic plate under the Northwest Pacific, hence the slab may preserve the original anisotropic property that the Pacific plate gained when it was produced in the mid-ocean ridge.

Wang and Zhao (2008) modified the tomographic method of Zhao et al. (1992) to obtain a much improved P-wave anisotropy tomography of the Tohoku subduction zone using 295,458 P-wave arrivals of 9308 local earthquakes in the crust and the subducting Pacific slab recorded by 311 seismic stations. They took into account the geometries of the Conrad and Moho discontinuities and the upper boundary of the subducting Pacific slab in the model, thus the theoretical travel times and ray paths can be computed more accurately (Zhao et al., 1992). Their results are in general agreement with those of Ishise and Oda (2005) but revealed more detailed features. They found that the anisotropic patterns are complex and different in the upper and lower crust. In the mantle wedge, the FVD is generally trench-parallel in the fore-arc area, whereas it becomes trench-normal in the back-arc area (Fig. 2), which agrees well with the SWS observations (Huang et al., 2011a,b). A trench-parallel FVD is revealed beneath the volcanic front, which may suggest the existence of complex 3-D mantle flow in the mantle wedge. The anisotropy is weaker in the upper crust (~1–2%) than that in the deeper areas, and the average amplitude of Vp anisotropy in the mantle is no larger than 4%.

These Vp anisotropy results have been confirmed and improved by later studies using better data sets for a few individual areas in Tohoku

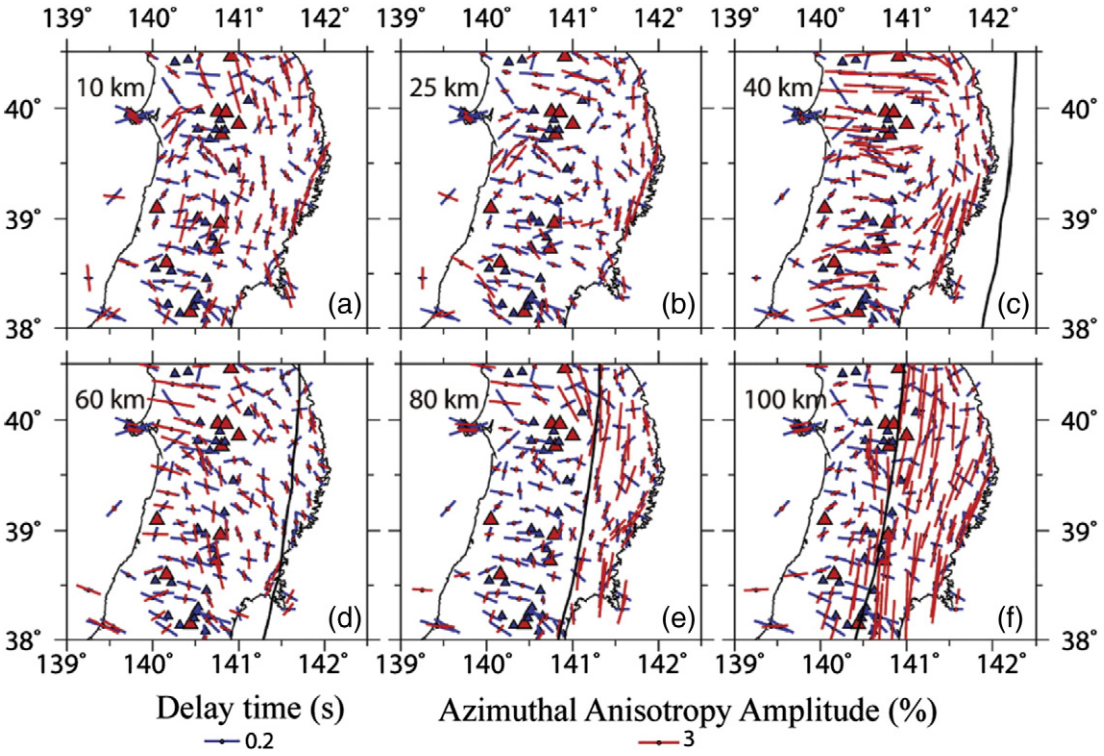

Fig. 2. Distribution of fast-velocity directions (FVDs; red bars) of P-wave azimuthal anisotropy beneath Northeast Japan. The depth of each layer is shown at the upper-left corner of each map. The blue bars denote shear-wave splitting measurements of local intermediate-depth earthquakes in the subducting Pacific slab by Huang et al. (2011a). The red and blue triangles denote the active and quaternary arc volcanoes, respectively. The azimuth of each bar represents the FVD, whereas the bar length denotes the S-wave delay time at each station or the P-wave anisotropy amplitude; their scales are shown at the bottom. The black curved lines denote the upper boundary of the subducting Pacific slab at each depth. After Wang and Zhao (2013).

and with more advances in technical details (Wang and Zhao, 2010; Cheng et al., 2011; Huang et al., 2011c; Wang and Zhao, 2013). Wang and Zhao (2010) and Huang et al. (2011c) extended their study regions to the entire Tohoku arc from the Japan Trench to the eastern margin of the Japan Sea by adding data from many suboceanic events which are relocated precisely with sP depth phases (Umino et al., 1995). They found that significant P-wave anisotropy also exists in the fore-arc area under the Pacific Ocean and the back-arc area beneath the Japan Sea.

The first tomography for Vp azimuthal anisotropy beneath Hokkaido of the southern Kuril arc was determined by Wang and Zhao (2009). Their model revealed P-wave anisotropy in the crust, mantle wedge and the subducting Pacific slab. In the upper crust, the anisotropy is possibly caused by micro-cracks and cracks. In the lower crust, the anisotropic structure is different from that in the upper crust and it may be affected considerably by the plastic flow deformation. In the mantle wedge, the Vp anisotropy results are quite similar to those in Tohoku, i.e., the FVD is generally trench-normal under the back-arc, but it becomes trench-parallel under the Pacific coast (fore-arc) area, which agrees with the SWS observations. Beneath the volcanic front, the FVD is also trench-parallel, suggesting a complex 3-D mantle flow in the mantle wedge. The FVD in the Pacific slab under Hokkaido is nearly north–south, which may reflect either the original fossil anisotropy of the Pacific plate formed at the mid-ocean ridge or the anisotropy is affected by the olivine fabric transition due to the changes in water content, stress and temperature (Wang and Zhao, 2009).

Detailed 3-D Vp and Vs tomography and P-wave anisotropy of the crust and upper mantle under Hokkaido from the Kuril–Japan trench to the eastern margin of Japan Sea were investigated by Liu et al. (2013). The suboceanic earthquakes used in the tomographic inversion were relocated precisely using sP depth-phase data which were collected from three-component seismograms recoded by the dense Japanese seismic network. Their results of P-wave azimuthal anisotropy beneath the Hokkaido land area are generally consistent with those of Wang and Zhao (2009). They also revealed significant anisotropy in the fore-arc area under the Pacific Ocean, which is similar to that beneath the Tohoku forearc (Wang and Zhao, 2010). Koulakov et al. (2015) presented a new Vp anisotropic tomography of the crust and upper mantle beneath Hokkaido. Their azimuthal anisotropy in the crust corresponds to the major tectonic units and delineates the major suture zones. In the mantle, the anisotropy has a fan-shaped configuration, which may reflect deviations of flows starting in southern Hokkaido and splitting into three directions. The western and eastern flows proceed toward the two volcanic groups on Hokkaido, and they may carry with them additional material to trigger the characteristic caldera-forming eruptions in these groups.

The first Vp radial anisotropy tomography was determined for the Tohoku arc using a large number of arrival-time data of local shallow and intermediate-depth earthquakes recorded by the dense seismic network (Fig. 3; Wang and Zhao, 2013). Their results show that Vpv > Vph in the mantle-wedge low-V zones under the arc volcanoes, which may reflect hot upwelling flows and transitions of olivine fabrics with the presence of water in the mantle wedge, due to the dehydration reactions of the Pacific slab. In contrast, Vpv < Vph in the subducting Pacific slab (Fig. 3), which, together with the azimuthal anisotropy results, suggest that the Pacific slab keeps its frozen-in anisotropy formed at the mid-ocean ridge, or the slab anisotropy is induced by LPO of the B-type olivine (e.g., Karato et al., 2008). Huang et al. (2015) examined the radial-anisotropy tomography beneath Tohoku and confirmed the main features revealed by Wang and Zhao (2013).

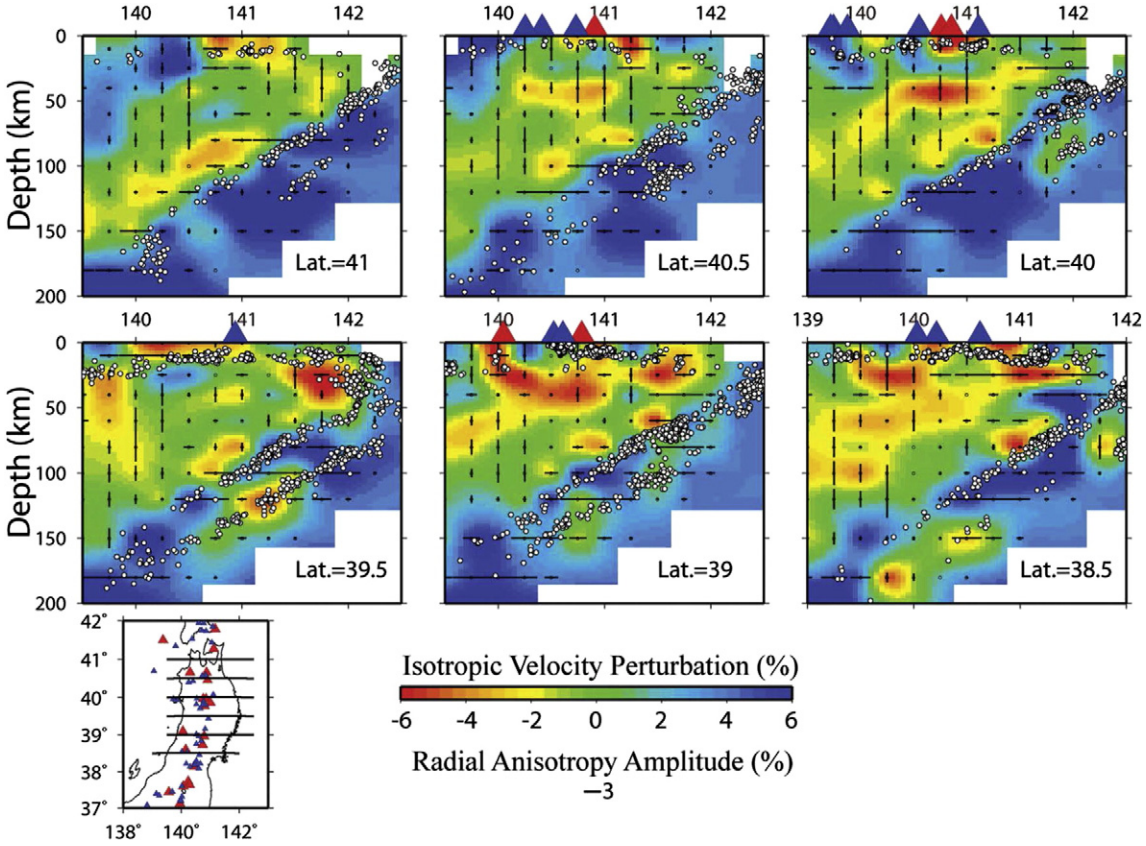

Fig. 3. East-west vertical cross-sections of P-wave radial anisotropy tomography beneath Northeast Japan along the profiles shown on the inset map (Wang and Zhao, 2013). The red and blue colors denote low and high isotropic-velocity anomalies, respectively. The horizontal bars denote that horizontal Vp > vertical Vp at each grid node, whereas the vertical bars denote that vertical Vp > horizontal Vp at each grid node. The bar length denotes the radial anisotropy amplitude; its scale is shown at the bottom. The red and blue triangles denote the active and quaternary arc volcanoes, respectively. The white dots denote the seismicity that occurred within a 10-km width of each profile.

3.2. Southwest Japan

In the SW Japan arc, the young Philippine Sea (PHS) slab is subducting beneath the Eurasian plate at the Nanak Trough at a rate of 3–5 cm/year. Many active and Quaternary arc volcanoes exist in SW Japan, and earthquakes occur actively in the crust and the subducting PHS slab down to ~200 km under Kyushu and down to ~80 km under Shikoku and Chugoku (e.g., Abdelwahed and Zhao, 2005; Tong et al., 2011; Zhao et al., 2011c; Liu and Zhao, 2014, 2015). Many tomographic studies have been made to study the 3-D Vp and Vs structures of the crust and upper mantle under SW Japan, which revealed the high-V and high-Q PHS slab and low-V and low-Q zones in the crust and upper-mantle wedge under the arc volcanoes (see Zhao, 2015a,b for detailed reviews). Recent teleseismic tomography shows that the PHS plate has subducted aseismically down to 460 km depth under the Japan Sea, Tsushima Strait and East China Sea, and a window exists within the aseismic PHS slab (Zhao et al., 2012; Huang et al., 2013). SWS measurements have been made, which revealed the existence of significant anisotropy in SW Japan (e.g., Ando et al., 1983; Kaneshima, 1990; Hiramatsu et al., 1997; Salah et al., 2008; Terada et al., 2013).

P-wave tomography for azimuthal anisotropy beneath SW Japan has been investigated by Ishise and Oda (2008) and Wang and Zhao (2012, 2013). These studies have obtained consistent results which show a complex pattern of Vp anisotropy in the crust and upper mantle. In Kyushu, the P-wave FVD is generally trench normal in the mantle wedge under the back-arc, which is consistent with the corner flow driven by the PHS slab subduction. The FVD is trench-parallel in the subducting PHS slab under Kyushu. Wang and Zhao (2012) suggested that the intraslab seismicity is a potential indicator to the slab anisotropy. That is, the PHS slab with seismicity has kept its original fossil anisotropy formed at the mid-ocean ridge, whereas the aseismic PHS slab has reproduced the anisotropy according to its current deformation.

Wang and Zhao (2013) determined high-resolution Vp tomographic images for both radial and azimuthal anisotropy under SW Japan. They revealed trench-normal FVDs in the back-arc mantle wedge under Kyushu, which reflects slab-driven corner flow in the mantle wedge. Trench-parallel FVDs are revealed in the fore-arc mantle wedge under Kyushu, suggesting the existence of a B-type olivine fabric there. This FVD pattern is consistent with the SWS measurements in Kyushu (e.g., Salah et al., 2008; Terada et al., 2013). Their result for Vp radial anisotropy is similar to that of the Tohoku arc, revealing that Vpv > Vph in the low-V zones in the mantle wedge under the arc volcanoes in Kyushu, as well as in the low-V zones below the PHS slab under SW Japan, which may reflect hot upwelling flows and transitions of olivine fabrics with the presence of water due to the slab dehydration. Trench-parallel FVDs and positive radial anisotropy (i.e., Vpv < Vph) are revealed in the PHS slab under Kyushu, which may indicate that the PHS slab keeps its frozen-in anisotropy formed at the mid-ocean ridge, or that the slab anisotropy is induced by LPO of the B-type olivine, similar to the Pacific slab under Tohoku (Wang and Zhao, 2013).

P and S wave tomography as well as Vp azimuthal anisotropy tomography in and around Japan were determined by inverting a great number of P and S wave arrival-times of local and regional earthquakes (Wei et al., 2015; Fig. 4). The results show some differences between Vp and Vs images for the stagnant Pacific slab in the mantle transition zone beneath NE China. The stagnant slab looks thicker in the Vp image than that in the Vs image, which may reflect the effects of both hydration and lower temperature in the mantle transition zone, though differences in the resolution of Vp and Vs tomography may also have some effects. The FVD in the subducting PHS plate beneath the Ryukyu arc is NE-SW (trench-parallel), which is consistent with the spreading direction of the West Philippine Basin during its initial opening stage, suggesting that it may reflect the fossil anisotropy. A striking variation of the FVD with depths is revealed in the subducting Pacific slab beneath the Tohoku arc, which may be caused by slab dehydration that changed elastic properties of the slab with depth. The FVD in the mantle wedge beneath the Tohoku and Ryukyu arcs is trench-normal, which reflects subduction-induced convection. Beneath the Kuril and Izu-Bonin arcs where oblique subduction occurs, the FVD in the mantle wedge is nearly normal to the moving direction of the downgoing Pacific plate, suggesting that the oblique subduction together with the complex slab morphology have disturbed the mantle flow (Fig. 4).

3.3. Mainland China

The structure and tectonics of Mainland China are affected by strong interactions among the Eurasian, Pacific, PHS and Indian plates. In and around China, there are many interesting and important geological and geophysical phenomena which are related to the fundamental scientific issues of solid-Earth sciences, such as the formation and evolution of active intraplate volcanoes (e.g., Changbai, Jeju, Wudalianchi, Tengchong and Hainan), the deep structure and fate of the subducting Pacific, Indian and PHS plates, lithospheric thinning and reactivation of the North China Craton (NCC), and the India-Asia collision (e.g., Wei et al., 2012; Zhao and Tian, 2013; Zhao, 2015a). Many researchers have studied the seismic structure and anisotropy of the crust and mantle beneath Mainland China to address the above-mentioned issues using various seismological methods, including travel-time tomography, surface-wave tomography, SWS measurements, and receiver functions (see Zhao, 2015a for a detailed review).

Archean cratons generally have a cold, old and thick lithosphere keel, and exhibit low heat flow and a lack of volcanism and large earthquakes. However, the NCC is an exception. It is the Chinese part of the Sino-Korean Craton and contains some of the oldest known continental rocks, being as old as 3.8 Ga. The NCC can be divided into two major Archean continental nuclei, that is, the NCC western block and the NCC eastern block, which are separated by a major lithospheric boundary in the NCC central block. Multidisciplinary studies have shown that the NCC eastern block has experienced significant lithospheric destruction from the Late Mesozoic to Cenozoic, in contrast to the long-term stabilization of the NCC western block (see a large number of related references cited in Tian and Zhao, 2013; Wang et al., 2013, 2014; Zhao, 2015a).

A Vp azimuthal anisotropy tomography of the crust and uppermost mantle beneath the NCC was determined using local-earthquake arrival times (Wang et al., 2013). The results show significant lateral heterogeneities beneath the NCC. The lower crust and uppermost mantle beneath the North China Basin show widespread low-V anomalies which may reflect high-temperature materials caused by the late Mesozoic basaltic magmatism in the NCC. Low-V anomalies also exist beneath the Trans-North China Orogen, which may reflect asthenospheric upwelling since the late Mesozoic. Large crustal earthquakes generally occurred in high-V zones in the upper to middle crust, whereas low-V and high-conductivity anomalies representing fluid-filled, fractured rock matrices exist in the lower crust to the uppermost mantle under the source zones of the large earthquakes. The crustal fluids may lead to the weakening of the seismogenic layer in the upper and middle crust and hence cause the large crustal earthquakes (e.g., Mishra and Zhao, 2003; Wang and Zhao, 2006; Sun et al., 2008; Lei and Zhao, 2009; Zhao et al., 2010; Padhy et al., 2011; Tong et al., 2011, 2012; Zhao et al., 2015). NW-SE P-wave FVDs are dominant in the uppermost mantle under the central parts of eastern NCC, suggesting that these mantle minerals were possibly regenerated but keep the original fossil anisotropy formed before the new lithospheric mantle was produced during the Mesozoic to Cenozoic (Wang et al., 2013).

A Vp anisotropy tomography beneath the NCC was determined using arrival-time data of local earthquakes and teleseismic events, revealing depth-dependent azimuthal anisotropy in the crust and upper mantle down to 600 km depth (Tian and Zhao, 2013). In the NCC western block, the FVD varies from E-W in the southern part to NE-SW in the northern part, which may reflect either the interaction between the Yangtze block and the NCC or fossil lithospheric fabrics in the craton. Beneath the NCC eastern block, a uniform NW-SE FVD is revealed in the

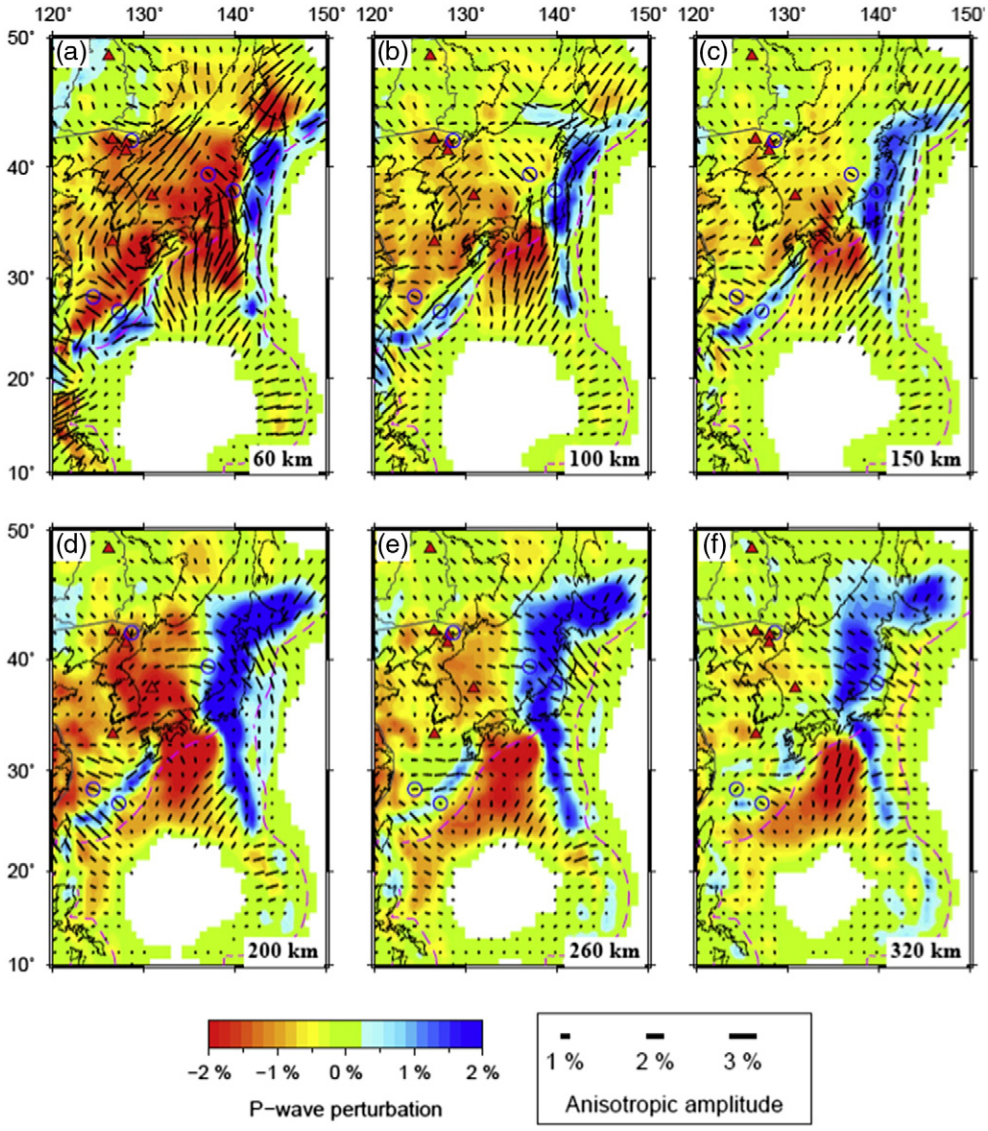

Fig. 4. Map views of P-wave azimuthal-anisotropy tomography beneath Western Pacific and East Asia. The layer depth is shown at the lower-right corner of each map. The red and blue colors denote slow and fast velocity perturbations, respectively. The azimuth and length of each bar represent the fast-velocity direction and anisotropic amplitude, respectively. The scales for the velocity perturbation and anisotropic amplitude are shown at the bottom. The red triangles denote active volcanoes. The dashed purple lines denote the plate boundaries. The five open circles denote the locations where P-wave ray azimuthal distributions are investigated in detail. After Wei et al. (2015).

asthenosphere (300–410 km depths) and the mantle transition zone (MTZ, 410–660 km depths), which may reflect horizontal and upwelling flows in the big mantle wedge above the stagnant Pacific slab in the MTZ. The NCC central block exhibits a NE-SW FVD, consistent with the surface tectonic orientation there, suggesting that the cold and thick (>300 km) cratonic root of the NCC western block may obstruct the NW-SE trending mantle flow induced by the Pacific plate subduction, resulting in a NE-SW trending mantle flow under the central block. These results indicate that the corner flow in the big mantle wedge associated with the deep subduction of the Pacific plate is the main cause of the NCC reactivation and mantle dynamics under East China, confirming the earlier tomographic results and the geodynamic model (Zhao et al., 2004; Lei and Zhao, 2005; Zhao et al., 2007).

A P-wave radial anisotropy tomography of the crust and upper mantle beneath the NCC was determined by Wang et al. (2014) using arrival-time data of local earthquakes and teleseismic events (Fig. 5). Their results show a prominent high-V anomaly down to ~250 km depth beneath the Ordos block, a high-V anomaly in the MTZ beneath the eastern NCC, and a low-V anomaly down to ~300 km depth beneath the Trans-North China Orogen. The Ordos block exhibits significant negative radial anisotropy (i.e., Vpv > Vph), suggesting that its cratonic lithosphere has kept the frozen-in anisotropy formed by vertical growth via high-degree melting mantle plume in the early Earth. Prominent low-V anomalies with positive radial anisotropy (i.e., Vph > Vpv) exist beneath the Qilian and Qaidam blocks down to ~400 km depth, suggesting that the horizontal material flow resulting from the Tibetan Plateau is blocked by the Ordos thick lithosphere. Beneath the eastern NCC, high-V anomalies with negative radial anisotropy exist in the upper mantle, possibly reflecting sinking remains of the Archean cratonic lithosphere. A high-V anomaly with positive radial anisotropy is revealed in the MTZ under the eastern NCC, which reflects the stagnant Pacific slab.

Vp tomography and azimuthal anisotropy of the crust and uppermost mantle beneath the Helan–Liupan–Ordos western margin tectonic belt in North-Central China were investigated using local-earthquake arrival-time data (Cheng et al., 2014) (Fig. 6). Significant Vp anisotropy is revealed in the study region, and the pattern of anisotropy in the upper crust is consistent with the surface geologic features. In the lower crust and uppermost mantle, the predominant FVD is NNE–SSW under the Yinchuan Graben and NWW–SEE or NW–SE beneath the Corridor transitional zone, Qilian Orogenic Belt and Western Qinling

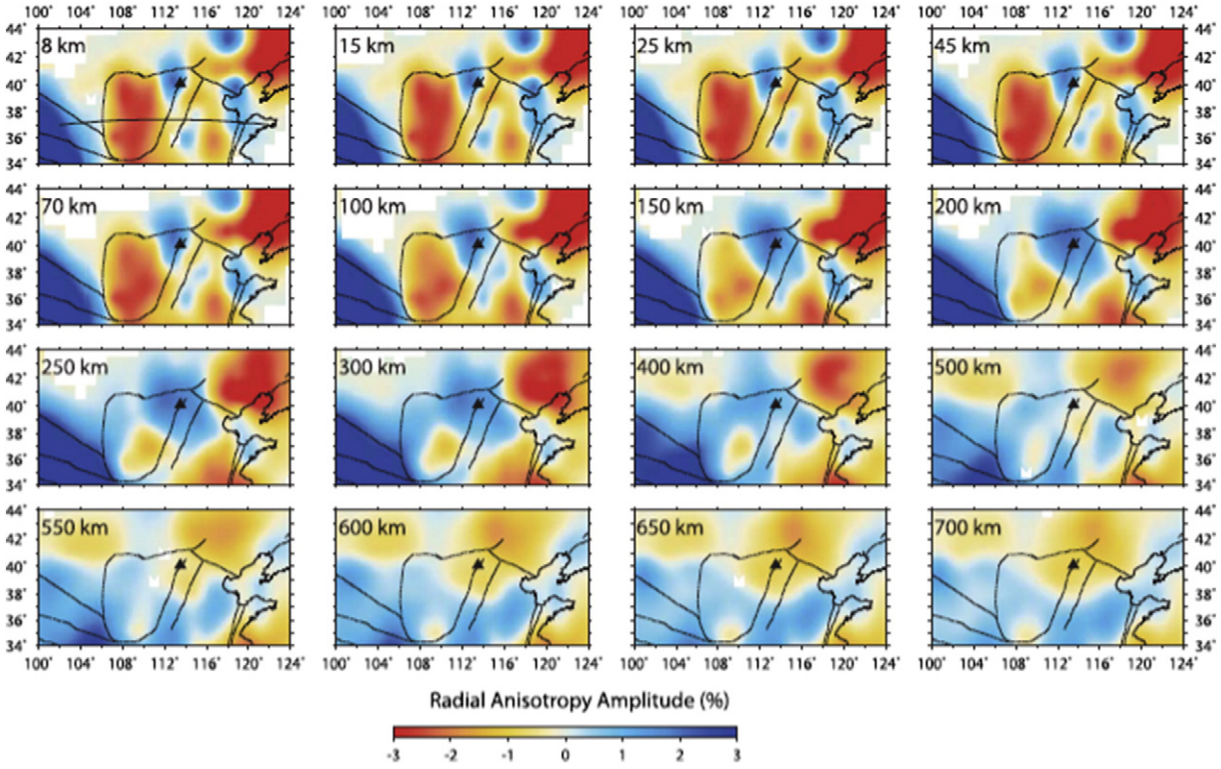

Fig. 5. Map views of radial anisotropy of P-wave velocity (Vp) beneath the North China Craton. The layer depth is shown at the upper-left corner of each map. The red color denotes negative radial anisotropy (i.e., vertical Vp > horizontal Vp), whereas the blue color denotes positive radial anisotropy (i.e., horizontal Vp > vertical Vp). The black lines show the major faults or block boundaries. The black triangle denotes the Datong volcano group. After Wang et al. (2014).

Orogenic Belt, and the FVD is NE–SW under the eastern Qilian Orogenic Belt (Fig. 6). The anisotropy in the lower crust may be caused by the LPO of minerals, which may reflect the ductile flow with varied directions.

Applying the method of Wang and Zhao (2008), Wei et al. (2013) determined a Vp azimuthal-anisotropy tomography beneath SE Tibet and adjacent regions using P-wave arrivals from local earthquakes and teleseismic events (Fig. 7). They revealed a remarkable low-V layer with a thickness of ~20 km in the lower crust, which may reflect a mechanically weak zone capable of flow on a geological timescale. Their Vp anisotropy results indicate that the flow direction changes when it encounters the mechanically strong Sichuan basin block. Most of the large earthquakes, including the 2008 Wenchuan earthquake (M 8.0) and the 2013 Lushan earthquake (M 7.0), occurred at the margin of the ductile flow in the lower crust, suggesting that the seismogenesis is controlled by the deep dynamic processes (Lei and Zhao, 2009; Wang et al., 2010). In the upper mantle, the subducting Indian plate is imaged clearly as a high-V zone which has reached the Jinsha River suture (He et al., 2010; Zhang et al., 2012). In addition, their results show significant variations of Vp anisotropy with depth, which suggests that the upper crust and the lithospheric mantle may have deformed separately beneath most parts of Eastern Tibet.

A 3-D model of Vp azimuthal anisotropy in the lithosphere beneath the entire Mainland China was determined using local-earthquake arrival-time data (Huang et al., 2014) (Fig. 8). The model shows that the FVDs are generally correlated with the surface geologic features, such as the strikes of the orogens, active faults, and tectonic boundaries. The FVDs in the upper crust are normal to the maximal horizontal stress (σH) in regions with extensive compression such as the Tibetan Plateau, whereas they are subparallel to σH in strike-slip shear zones such as the western and eastern Himalayan syntax. Beneath the Tibetan Plateau, the seismic anisotropy in the lithosphere contributes significantly to the SKS splitting observations. In contrast, in eastern China the P-wave FVDs in the lithosphere are different from the SKS splitting measurements, suggesting that the SKS splitting is mainly caused by the anisotropy in the asthenosphere and the MTZ under eastern China.

3.4. Indonesia

At the Java-Sunda trench the Indian-Australian plate is subducting beneath the Eurasian plate. This is one of the most seismically active regions in the world, with earthquakes occurring from the surface to the base of the MTZ. Koulakov et al. (2009) studied Vp and Vs tomography and 3-D Vp anisotropy structure of the crust and upper mantle down to ~150 km depth beneath central Java using local-earthquake arrival-time data recorded by a local seismic array (Fig. 9). For the Vp anisotropic model, they determined four parameters for each parameterization cell, which represent an orthorhombic anisotropy with one predefined direction oriented vertically. Three of the parameters describe slowness variations along three horizontal orientations with azimuths of 0, 60 and 120 degrees, and one is a perturbation along the vertical axis. Their results show that the crustal and uppermost mantle Vp structure beneath central Java is strongly anisotropic with 7–10% of maximal difference between slow and fast Vp in different directions. In the forearc area between the southern coast and the Java arc volcanoes, both isotropic and anisotropic structures are strongly heterogeneous. The FVD variations and highly contrasted velocity patterns can be explained by a complex block structure of the crust. Beneath the Java arc volcanoes, they revealed faster velocities in vertical direction, which is probably an indicator for vertically oriented structures (channels, dykes). In the crust beneath the middle part of central Java, north to Merapi and Lawu volcanoes, they found a large and very intense anomaly with a velocity decrease of up to 30% and 35% for the Vp and Vs models, respectively. Inside this anomaly the FVD is E-W, probably caused by regional extension stress regime. In a vertical cross-section, faster horizontal Vp is revealed inside this anomaly that might be explained by layering of sediments and/or penetration of quasi-horizontal lenses with molten magma. In the mantle, trench-

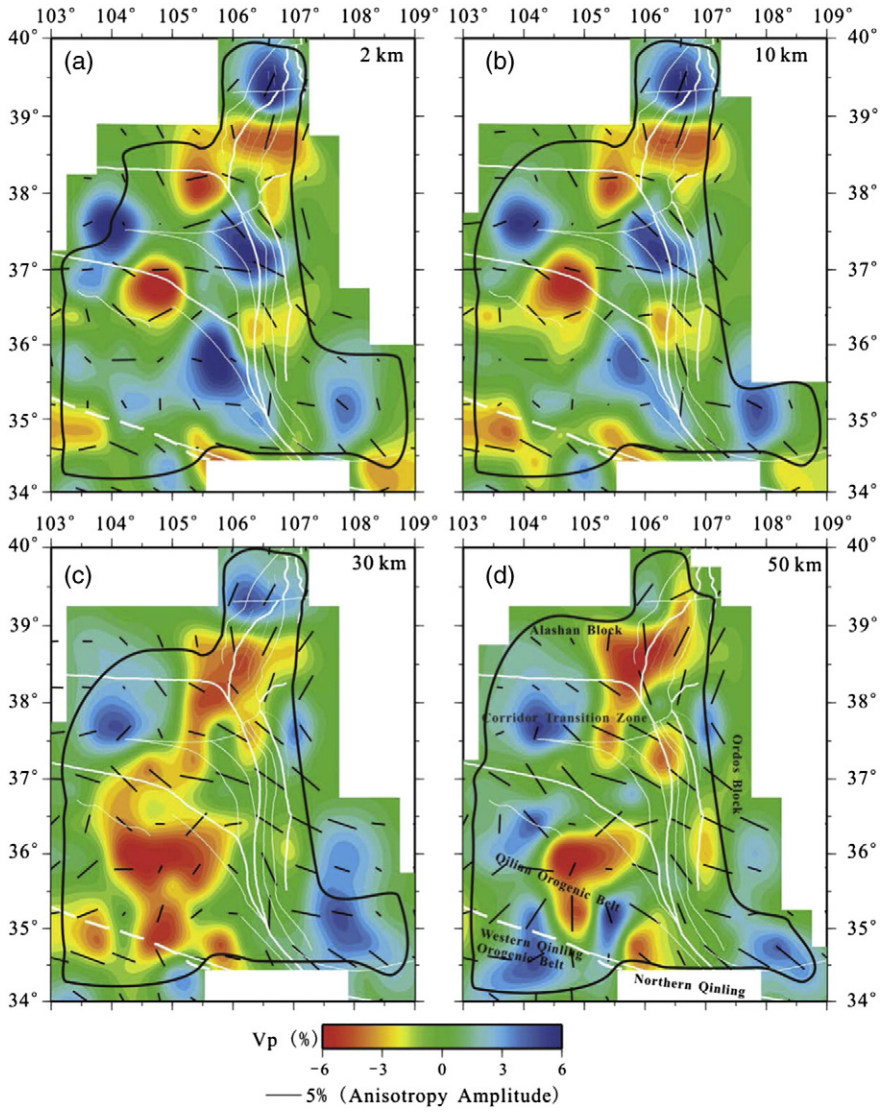

Fig. 6. Map views of P-wave azimuthal-anisotropy tomography beneath North-Central China (Cheng et al., 2014). The depth of each layer is shown at the upper-right corner of each map. The red and blue colors denote low and high velocities, respectively. The orientation and length of the bars represent the fast-velocity direction and anisotropic amplitude with its scale shown at the bottom. The white solid lines denote the active faults, whereas the dashed white line denotes the Shangdan suture zone (SDSZ). The black lines delineate the region where the tomographic result is reliable according to the resolution analysis.

parallel anisotropy is observed throughout the study area. Such an anisotropy in the slab-entrained corner flow may be due to presence of B-type olivine having predominant axis parallel to the shear direction, which appears in conditions of high water or/and melt content (Koulakov et al., 2009). This Vp anisotropic model can generally explain the SWS measurements made in the same region (Hammond et al., 2010).

3.5. New Zealand

New Zealand is a well-studied subduction zone where the Pacific plate is subducting beneath the Australian plate in North Island. Various seismological methods have been applied to study the 3-D crust and upper mantle structure of the region (for recent reviews, see Reyners, 2013; Eberhart-Phillips et al., 2013). Eberhart-Phillips and Henderson (2004) conducted Vp azimuthal-anisotropy tomography for the central New Zealand. They used the fast polarization directions from local-earthquake SWS (Audoine et al., 2000) to define an initial anisotropy model. The ray paths are estimated for each of the SWS observations and the 3-D initial model is determined via an averaging process and a coherence analysis. The initial magnitude of anisotropy at a node is dependent on the number of adjacent ray paths and the consistency of the SWS measurements. A blended approach is used to damp the perturbations to the magnitude of anisotropy and/or perturbations to the FVD. They applied this approach to the Marlborough region in central New Zealand, and their results show variations in P-wave anisotropy in the brittle upper crust, ductile lower crust, mantle wedge and the subducting Pacific slab. The patterns are consistent with the SWS observations (Klosko et al., 1999; Audoine et al., 2000, 2004), but show some additional features. The maximum anisotropy is approximately 12% oriented northeast, between the Awatere and Wairau faults. This strong anisotropy may reflect deformation and extensive fracturing in a region of high total shear strain. In the region of interaction of the ductile lower crust with the shallow subducting slab, moderate anisotropy with east–west orientation is imaged, which is consistent with ductile deformation roughly parallel to the plate velocity.

A Vp anisotropy tomography in the central North Island, New Zealand was determined using local-earthquake arrival-time data (Eberhart-Phillips and Reyners, 2009). The results suggest that mantle flow, either within the mantle wedge or below the subducted slab, is not the primary source of anisotropy in the Hikurangi subduction zone. The strongest anisotropy was revealed within the subducting Pacific slab, where the FVD is consistently trench-parallel and the strength

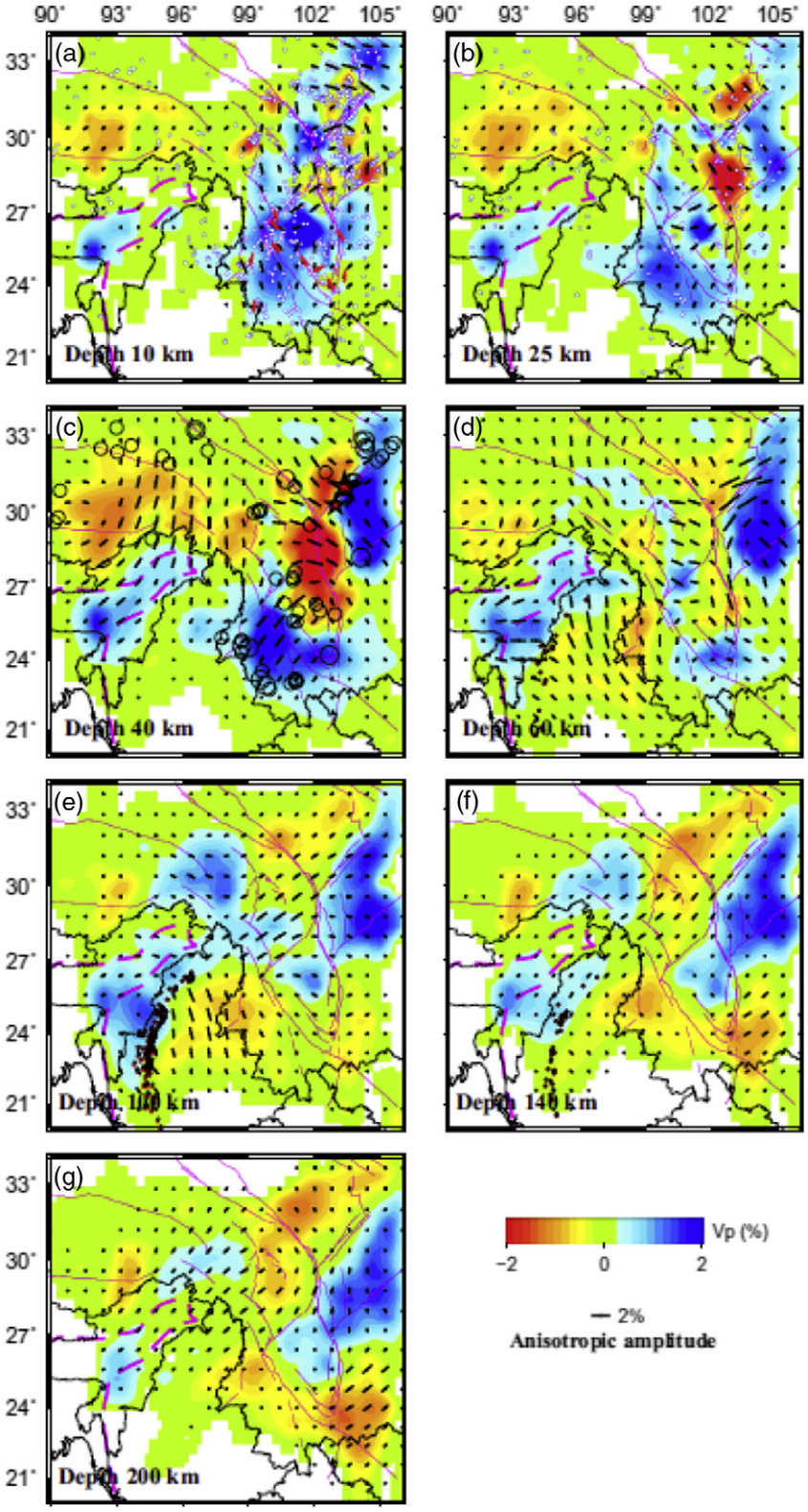

Fig. 7. Map views of P-wave azimuthal-anisotropy tomography beneath Eastern Tibetan Plateau (Wei et al., 2013). The layer depth is shown at the lower-left corner of each map. The red and blue colors denote slow and fast velocity perturbations, respectively. The azimuth and length of each bar represent the fast-velocity direction and anisotropic amplitude, respectively. The red bars in (a) show the results of shear-wave splitting measurements of local earthquakes (Shi et al., 2006). The scales for the velocity perturbation and anisotropic amplitude are shown below (f). The black open circles in(c) represent the large crustal earthquakes (M > 6.0) that occurred since 1970. The white and red dots show background seismicity in the crust and the intermediate-depth earthquakes, respectively. The large and small red stars in (c) represent the 2008 Wenchuan earthquake (M8.0) and the 2013 Lushan earthquake (M7.0), respectively. The pink lines show the large active faults and sutures in the study region. The purple dashed lines show the plate boundaries.

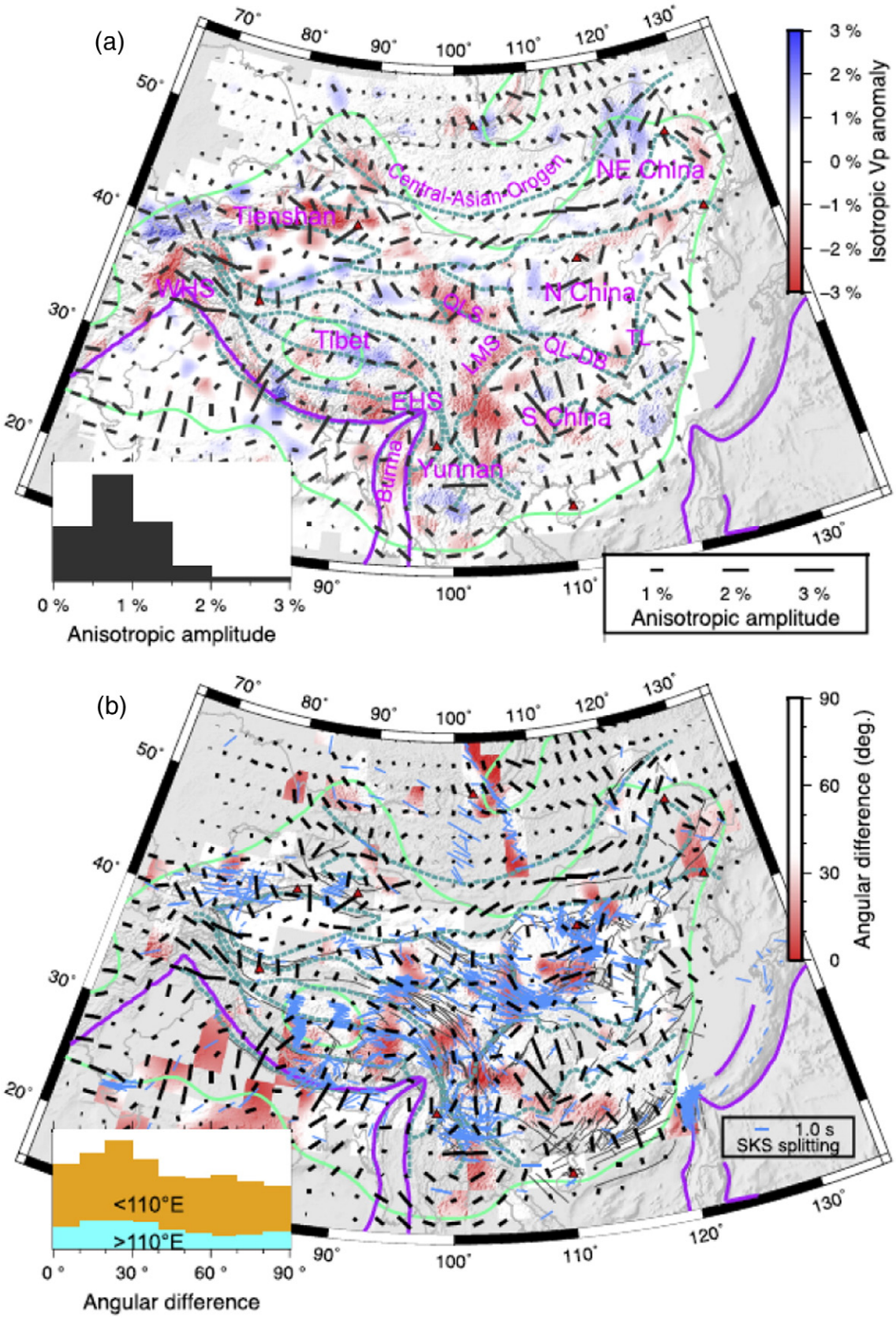

Fig. 8. (a) Map view of P-wave azimuthal-anisotropy tomography at 40 km depth beneath Mainland China. The blue and red colors denote high and low isotropic velocities, respectively. The orientation and length of the short bars represent the fast velocity direction (FVD) and anisotropic amplitude of P-wave azimuthal anisotropy, respectively. The bold green contours show the areas with degree of recovery R ≥ 0.5. The scale for the isotropic velocity anomaly is shown on the right, and the scale for the anisotropic amplitude is shown at the bottom-right inset. The histogram in the bottom-left inset shows the statistics of the anisotropic amplitudes. (b) Comparison of the P-wave FVDs (black bars) with SKS splitting measurements (blue bars). The red color denotes areas where the P and S wave FVDs are subparallel to each other (i.e., the angular difference between them is < 30°). The scale for the angular difference is shown on the right. The orange and blue histograms in the bottom-left denote the statistics of the angular differences to the west and east of 110°N, respectively. The purple curves denote the boundaries of the five major plates and the blocks in and around China. The gray curves denote the active faults. The red triangles denote the active intraplate volcanoes. After Huang et al. (2014).

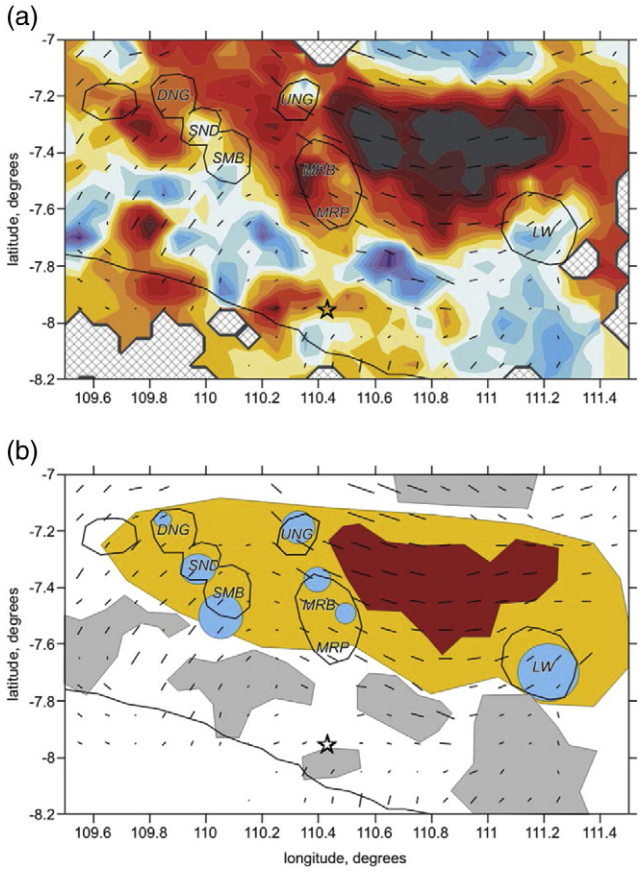

Fig. 9. (a) Distribution of isotropic and anisotropic P-wave velocity anomalies at 5 km depth beneath central Java. The red and blue colors denote low and high isotropic-velocity anomalies, respectively. The orientation and length of the short bars denote the fast velocity direction and strength of P-wave azimuthal anisotropy. The star indicates the epicenter of the 2006 Bantul Mw 6.5 earthquake. (b) Interpretation of the tomographic image in (a). The dark red area shows an anomaly with an extremely strong amplitude. The yellow area is supposed as feeding the volcanoes in central Java. The blue circles are placed over locally higher-velocity anomalies which may reflect the position of magmatic intrusions frozen in volcanic channels and reservoirs. Grey areas are placed over the high-velocity anomalies in the fore-arc and may reflect rigid crustal blocks surrounded by folded belts. After Koulakov et al. (2009).

of Vp anisotropy is 5–9% from 32 to 185 km depth. Bending-induced yielding in the slab offshore and as it passes through the trench provides an explanation for this slab anisotropy. Beneath the Taupo Volcanic Zone (TVZ), there is 1–4% trench-normal anisotropy within 30 km of the surface of the slab, within a region entrained with motion of the slab. In contrast, only very weak (0–2%) anisotropy is imaged in the region of high-temperature partial melt arising from active corner flow in the mantle wedge. In the crust geologic structure is important, with the largest crustal anisotropy (14%) related to schist. Significant anisotropy aligned with the margins of the TVZ was revealed, which may be related to extensive fracturing on the margins as the TVZ actively extends. Within the heavily intruded and underplated TVZ lower crust, the FVD switches to align with the extension direction, which is consistent with other geophysical data suggesting the presence of connected melt in this region (Eberhart-Phillips and Reyners, 2009).

The feature of weak anisotropy in the mantle wedge but strong anisotropy in the crust and the subducting slab beneath New Zealand is similar to the result of the Tohoku arc revealed by SWS measurements of local earthquakes in the upper crust, low-frequency microearthquakes in the lower crust and uppermost mantle, as well as intermediate-depth earthquakes within the upper and lower planes of the double seismic zone within the subducting Pacific slab (Huang et al., 2011a,b).

3.6. Alaska

In South-Central Alaska, the Pacific plate is subducting beneath the North American plate, causing active seismicity and arc volcanism along the Alaska-Aleutian subduction zone. In the past two decades many researchers have investigated the 3-D crustal and upper mantle structure of the Alaska subduction zone using various seismological methods, revealing the high-V subducting Pacific slab and low-V anomalies in the crust and upper-mantle wedge associated with the arc magmatism (for details, see Tian and Zhao, 2012a; Wang and Tape, 2014).

Tian and Zhao (2012a) determined Vp and Vs tomography and 3-D P-wave azimuthal anisotropy of the Alaska subduction zone using arrival times of local shallow and intermediate-depth earthquakes recorded by the dense seismic network deployed in South-Central Alaska (Fig. 10). They revealed the high-V Pacific slab and low-V anomalies in the mantle wedge with significant along-arc variations beneath the active arc volcanoes, which are consistent with previous isotropic Vp tomography under the region (e.g., Zhao et al., 1995; Qi et al., 2007). Significant Vp anisotropy is revealed, and the predominant FVD is trench-parallel in the shallow part of the mantle wedge (<90 km depth) and in the subslab mantle, whereas the FVD is trench-normal within the subducting Pacific slab (Fig. 10). This FVD pattern is consistent with the SWS measurements (Christensen and Abers, 2010). The trench-parallel FVDs in the mantle wedge and subslab mantle reflect the 3-D mantle flow induced by the complex geometry and strong curvature of the Pacific slab, as well as its flat and oblique subduction under Alaska. The trench-normal FVD within the Pacific slab may reflect the original fossil anisotropy when the Pacific plate was produced at the mid-ocean ridge (Tian and Zhao, 2012a). This result for the slab anisotropy beneath Alaska is the same as those beneath the Japan and Kuril arcs (Ishise and Oda, 2005; Wang and Zhao, 2012, 2013; Liu et al., 2013).

Teleseismic Rayleigh waves were used to image large-scale variations in Vs structure and anisotropy beneath South-Central Alaska (Wang and Tape, 2014). Their imaging technique employs a two-plane wave representation with finite-frequency sensitivity kernels. Their 3-D isotropic Vs model reveals several features: the high-V subducting Pacific/Yakutat slab, low-V anomalies characterizing the onshore Yakutat collision zone, the low-V Wrangell subduction zone, and a deep tomographic contrast at the eastern edge of the Pacific/Yakutat slab. Their anisotropic phase-velocity images exhibit variations in the FVD of azimuthal anisotropy, which show the dominance of the Yakutat slab on the observed pattern of anisotropy. West of the Yakutat slab the FVDs are approximately aligned with the plate convergence direction. In the region of the Yakutat slab the pattern is more complicated. Along the margins of the slab the FVDs are roughly parallel to the margins. There are notable differences and similarities with the SKS splitting measurements (Christensen and Abers, 2010).

3.7. North America

The deployment of the EarthScope/USArray since 2004 has greatly improved our understanding of the mantle structure and dynamics beneath the United States (US). Many high-resolution seismic images have been obtained and we are beginning to narrow down the mantle structure, particularly beneath the western US, to the scale of ~200 km (e.g., Becker, 2012; Chen et al., 2014, 2015). The tectonic involution of western US, including the active subduction of the Juan der Fuca plate, extensive subduction-related volcanism and intraplate volcanism (e.g., the Yellowstone hotspot), as well as mountain building, was thoroughly discussed and many models have been proposed on the basis of slab-mantle interactions revealed by the seismic images (e.g., Becker, 2012; Tian and Zhao, 2012b; Chen et al., 2015).

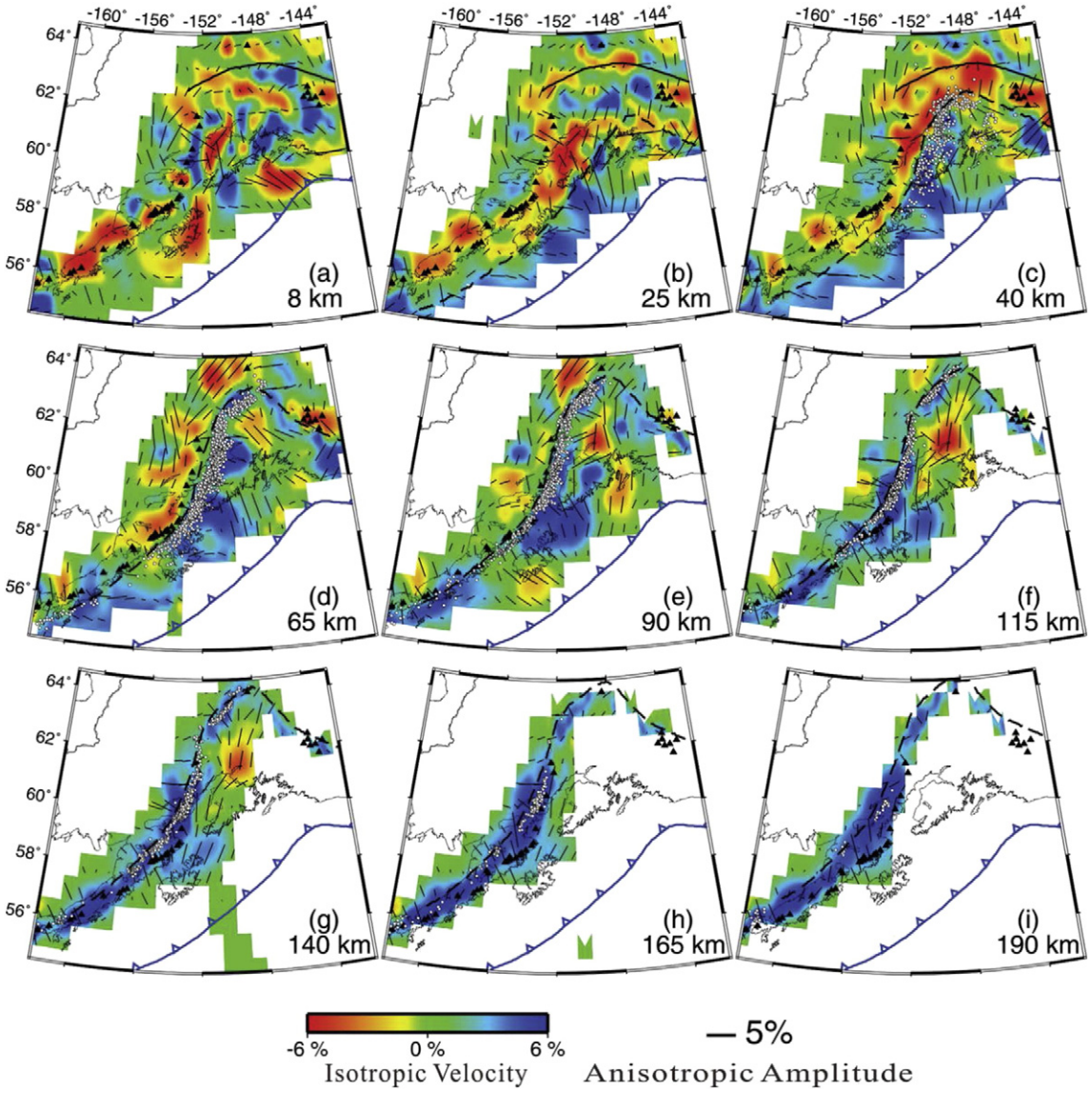

Fig. 10. Map views of P-wave azimuthal-anisotropy tomography of the Alaska subduction zone (Tian and Zhao, 2012a). The red and blue colors denote slow and fast isotropic velocities, respectively. The short lines denote fast-velocity directions of azimuthal anisotropy. The scales for the isotropic velocity and anisotropic amplitude are shown at the bottom. The black triangles denote active arc volcanoes. The blue sawtooth lines denote the trench. The dashed lines indicate the upper boundary of the Pacific slab at each depth. The grey dots show the earthquakes occurring in the subducting Pacific slab.

A large number of arrival-time data from local earthquakes and teleseismic events recorded by the USArray were used to determine a 3-D Vp model of azimuthal anisotropy tomography of the crust and upper mantle beneath the US (Huang and Zhao, 2013) (Fig. 11). The results show that FVDs in the lithosphere under the tectonically active areas correlate well with the surface tectonic features, suggesting that the Vp anisotropy mainly reflects the present deformation. A circular pattern of the FVDs centered in the Great Basin is revealed, which is well consistent with the specific circular SWS observations there (Wustefeld et al., 2009), suggesting that the anisotropy occurs in the crust and uppermost mantle. In contrast, beneath the stable cratonic region, the FVDs revealed by Huang and Zhao (2013) differ from the SWS observations but consistent with the features of gravity and magnetic anomalies, indicating that the P-wave FVDs mainly reflect the fossil anisotropy in the lithosphere, whereas the SWS observations mainly reflect the significant anisotropy in the asthenosphere. These P-wave anisotropy results shed new light on the seismic anisotropy in the crust and upper mantle and provide new constraints on constructing geodynamic models beneath the US.

3.8. Central America

The tectonic setting of Central America is characterized by the subduction of the Cocos plate beneath the Caribbean plate (e.g., Rabbel et al., 2011). The Cocos plate shows strong structural variations within relatively short distances. Lateral changes along the volcanic arc of the overriding Caribbean plate are a consequence of lateral changes in the structure, age and composition of the incoming oceanic Cocos plate (e.g., Carr et al., 2007; Rabbel et al., 2011). The incoming plate consists of three segments (von Huene et al., 1995): (1) a smooth segment of regular oceanic lithosphere with long trench-parallel fractures off northern Costa Rica (Nicoya Peninsula segment) continuing to Nicaragua, (2) a topographically rough segment covered with seamounts off central Costa Rica (Jaco-Quepos segment), and (3) the thickened and rough oceanic lithosphere of the Cocos Ridge subducting beneath southern Costa Rica (Osa Peninsula segment). A corresponding segmentation is revealed along the arc of the overriding plate. It is volcanically active along the projection of sections 1 and 2 but shows major geochemical differences in the magmas between 1 and 2 (Carr et al.,

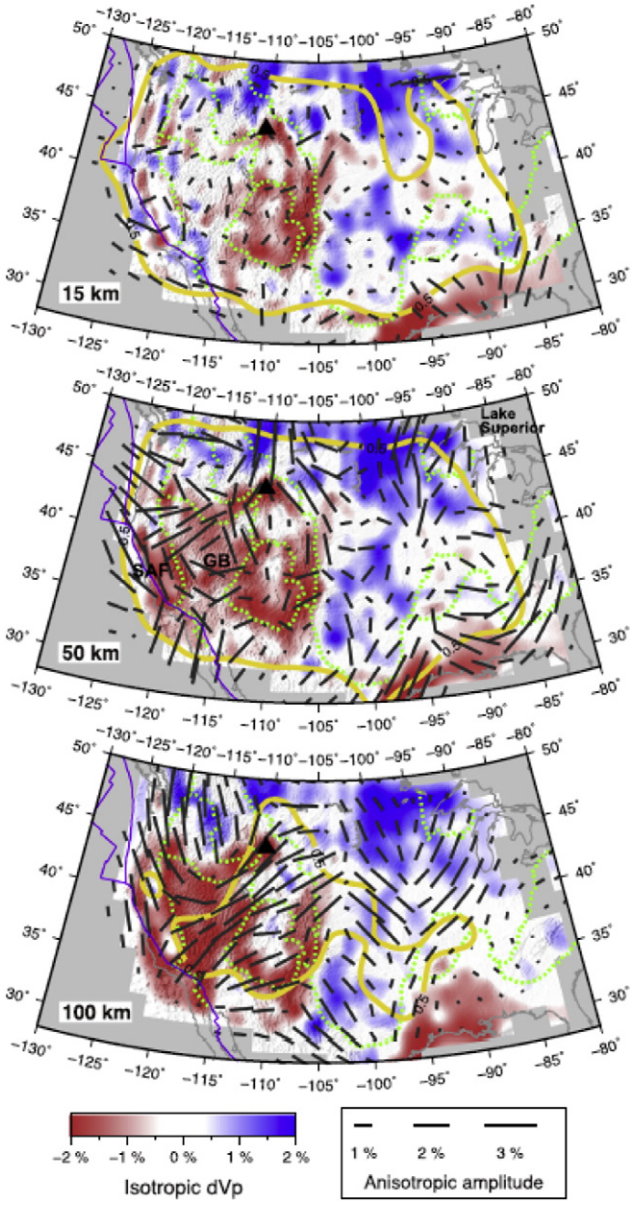

Fig. 11. Map views of P-wave azimuthal-anisotropy tomography beneath USA (Huang and Zhao, 2013). The depth of each image is shown at the lower-left corner of each map. The blue and red colors denote high and low isotropic velocities, respectively. The orientation and length of the short bars represent the fast-velocity direction and anisotropic amplitude of azimuthal anisotropy, respectively. The bold yellow contours show the areas where the azimuthal anisotropy is well resolved. The scales for the isotropic-velocity anomaly and the anisotropic amplitude are shown at the bottom. The purple curves denote the plate boundaries. The dashed green curves show different tectonic blocks in North America. The black triangle shows the Yellowstone hotspot.

2007). Above the subducting Cocos Ridge the Talamanca mountain range formed where the active volcanism stopped in the Late Miocene, showing a recent uplift rate of up to 4.7 mm/year (Gardner et al., 1992; Rabbel et al., 2011).

Rabbel et al. (2011) determined a 3-D Vp anisotropy tomography of the Central America subduction zone (Fig. 12). In the upper crust beneath Costa Rica, the anisotropy shows strong lateral variations corresponding to the complicated tectonic structure. In the upper mantle, the anisotropy exhibits a more coherent FVD that varies systematically at regional scales. The upper mantle of the incoming Cocos plate exhibits a trench-normal FVD, which may reflect mineral LPO in the transport direction. This pattern changes in the uppermost part of the subduction zone, which may be affected by bending-related trench-parallel faults and serpentinization that can overprint or change the LPO. The overriding Caribbean plate and the mantle wedge show a clear trench-parallel FVD. The Vp anisotropy is stronger in Nicaragua than that in southern central Costa Rica, which may be caused by a change in the stress regime from compressional in southern Costa Rica to transpressional in Nicaragua, corresponding to a change from a near-orthogonal subduction in the SE to an oblique subduction and slab retreat in the NW. The obtained Vp anisotropy in the mantle wedge reflects LPO associated with a trench-parallel shear deformation and/or NW oriented escape flow produced in the compressional zone near the Cocos Ridge collision area (Rabbel et al., 2011).

4. Shear-wave splitting tomography

A simple method of 3-D SWS tomography was proposed to image the spatial anisotropy distribution by back-projecting SWS delay times along ray paths derived from a 3-D Vs model, assuming the delay times are accumulated along the ray paths (Zhang et al., 2007). The local strength of the anisotropy is expressed by a parameter of anisotropy percentage, K. Using the SWS delay times for 575 earthquakes measured at two stations, they imaged a 3-D anisotropy percentage model around the San Andreas Fault Observatory at Depth (SAFOD). Li et al. (2014) used this method to estimate the spatial distribution of crustal anisotropy in the Karadere–Düzce branch of the North Anatolian Fault (NAF) in western Turkey.

Note that a critical problem in the method of Zhang et al. (2007) is that only the SWS delay times are taken into account in the tomographic inversion, whereas the fast polarization directions of SWS measurements are neglected. In other words, this method is only available when the fast polarization directions are the same for all the SWS measurements, and the fast directions are the same at all depths beneath a study area, which are quite rare in actual studies.

Abt and Fischer (2008) presented another method of SWS tomography by parameterizing the upper mantle as a 3-D block model of crystallographic orientations with the elastic properties of olivine and orthopyroxene, and both orthorhombic and hexagonal symmetries are tested. To efficiently forward calculate splitting, the Christoffel equation is used to progressively split the horizontal components of a synthetic wavelet in each block of the model, and predicted SWS parameters are obtained with an eigenvalue minimization technique. Numerically calculated partial derivatives are utilized in a linearized, damped least-squares inversion to solve for a best-fitting model of crystallographic orientations. To account for the non-linear properties of SWS, the inversion is applied iteratively and partial derivatives are recalculated after each iteration. Abt et al. (2009) applied this SWS tomography method to determine a 3-D model of crystallographic orientation in the mantle wedge beneath Costa Rica and Nicaragua (Fig. 13). Their best-fitting model contains roughly horizontal, arc-parallel olivine [100] axes in the mantle wedge down to at least 125 km depth beneath the back arc and arc, which may reflect along-arc flow in the mantle wedge. Pb and Nd isotopic ratios in arc lavas provide additional evidence for arc-parallel flow and also constrain the direction (northwest, from Costa Rica to Nicaragua) and minimum flow rate (6.3–19 cm/year). With only slightly oblique subduction at 8.5 cm/year of the relatively planar Cocos plate, the most likely mechanism for driving along-arc transport is toroidal flow around the edge of the slab in southern Costa Rica, generated by greater slab rollback in Nicaragua. Two implications of this arc-parallel flow are the progressive depletion of the mantle source for arc lavas from Costa Rica to Nicaragua and the possible need for significant decoupling between the wedge and the subducting slab.

Monteiller and Chevrot (2011) developed an approach for imaging SWS anisotropy, which relies on finite-frequency effects in the splitting of *SKS* waves. They built a data set of ~3400 *SKS* splitting measurements at all the broad-band stations in southern California. Resolution tests demonstrate that they could resolve anisotropic structures smaller than the size of the first Fresnel zone of *SKS* waves. The good vertical

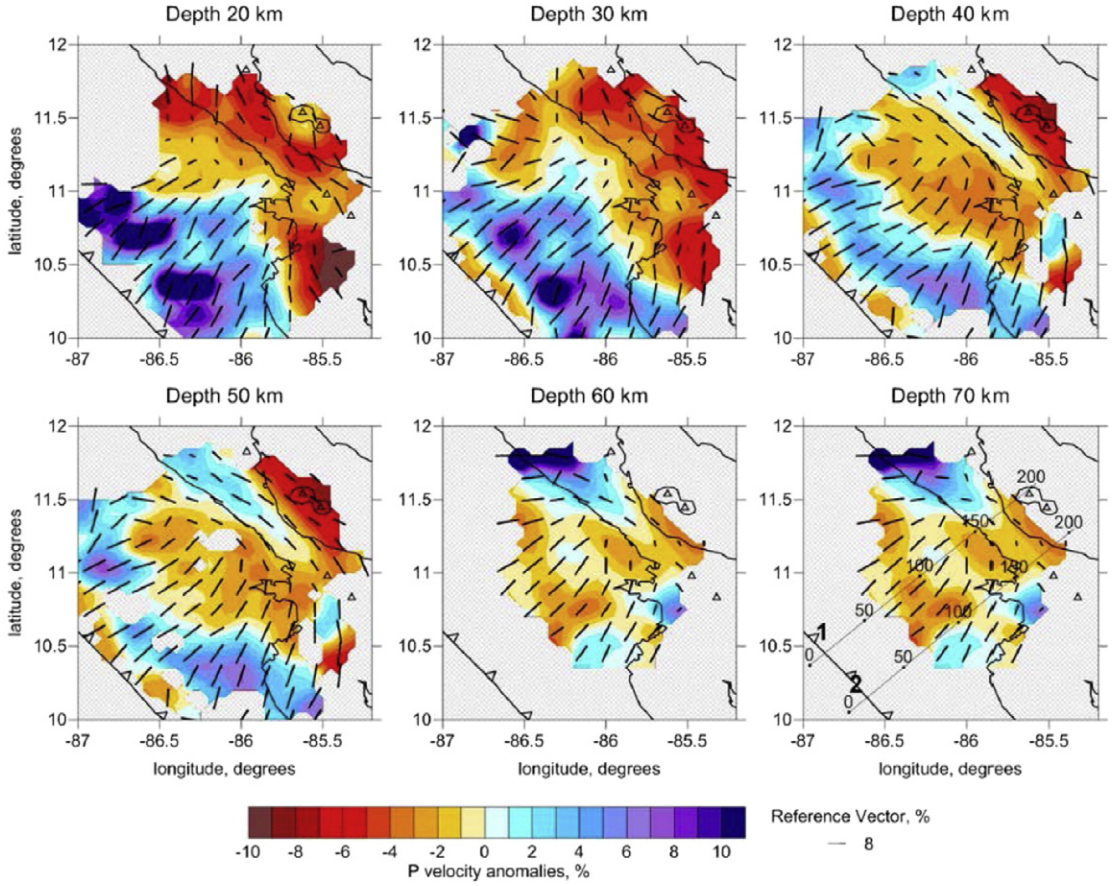

Fig. 12. Map views of the P-wave anisotropic tomography of the Central America subduction zone. The red and blue colors indicate low and high isotropic-velocity perturbations with their scale shown at the bottom. The bars show the directions of maximum horizontal velocities. The lengths of the bars show the amplitude of the velocity anisotropy with its scale shown at the bottom. The sawtooth line denotes the trench axis. After Rabbel et al. (2011).

resolution in their tomographic images results from the short interstation spacing in southern California. Their 3-D anisotropy model shows no evidence for localized lithospheric shear deformation beneath the San Andreas Fault. Instead, the lithospheric plate boundary is localized along a broad shear zone beneath the East California Shear Zone. Therefore, surface and deep deformation patterns are poorly correlated and most likely decoupled. Active N–S convergence in the Transverse Ranges results in strongly coherent E–W alignment of olivine fast

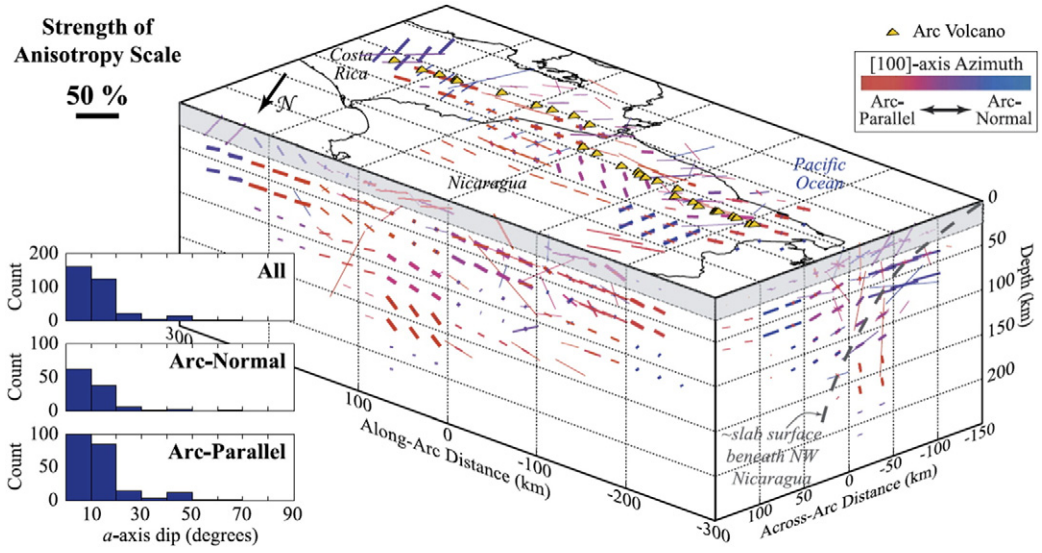

Fig. 13. Pseudo-3-D view of shear-wave anisotropy beneath Nicaragua and Costa Rica obtained by inverting shear-wave splitting measurements (Abt et al., 2009). All well-resolved model *a* axes of olivine (color bars) are projected onto an along-arc, an across-arc, and a horizontal plane. The color of the bars represents azimuth and varies from arc-parallel (red) to arc-normal (blue). The thickness of the bars is scaled by the resolution: thicker bars are better resolved, whereas thinner bars are less well resolved. The dip of arc-parallel (arc-normal) *a* axes can be seen in the along-arc (across-arc) cross-section. Histograms of *a* axis dip are shown to the left, and nearly all well-resolved *a* axes have dips less than 20°. The gray masking of the top layer means that the crustal anisotropy cannot be interpreted well.

axes in the shallow lithosphere. At the top of the asthenosphere, the observed low level of anisotropy suggests weak lithospheric basal tractions and thus a strong decoupling between the lithosphere and the asthenosphere.

Lin et al. (2014) applied a full-wave approach to image the upper-mantle anisotropy in Southern California using 5954 SKS splitting data. They adopted 3-D sensitivity kernels combined with a wavelet-based model parameterization in a multiscale inversion. Spatial resolution lengths were estimated based on a statistical resolution matrix approach, showing a finest resolution length of ~25 km in regions with densely distributed stations. Their anisotropic model displays structural fabric in relation to surface geologic features such as the Salton Trough, the Transverse Ranges, and the San Andreas Fault. The depth variation of anisotropy does not suggest a lithosphere-asthenosphere decoupling proposed by Monteiller and Chevrot (2011). At long wavelengths, the fast directions of anisotropy are aligned with the absolute plate motion inside the Pacific and North American plates (Lin et al., 2014).

Combining long-period seismic waveforms and SKS splitting measurements, Yuan et al. (2011) determined a 3-D upper-mantle tomographic model of North America that includes isotropic Vs with a

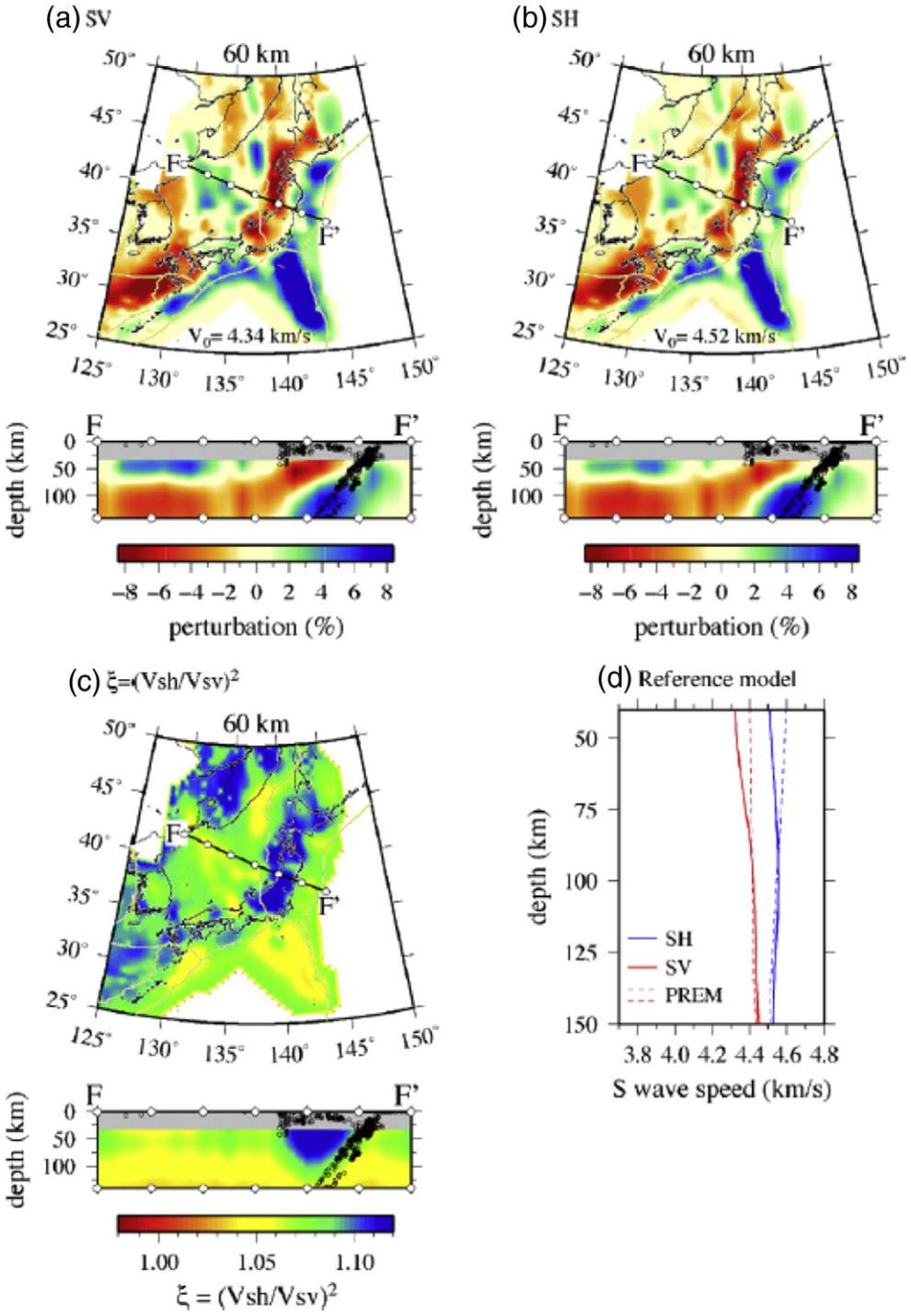

Fig. 14. Anisotropic shear-wave velocity models at 60 km depth and vertical cross-sections (Yoshizawa et al., 2010). (a) SV-wave velocity, (b) SH-wave velocity, and (c) radial anisotropy parameter $\xi = (VSH/VSV)^2$. White circles on the frame of each cross-section are plotted every 2°. (d) The average of SV and SH wave velocity models (solid lines) used as reference models in (a) and (b), and the SH and SV wave velocity of anisotropic PREM (dashed lines).

lateral resolution of ~250 km, as well as radial and azimuthal anisotropy with a lateral resolution of ~500 km. Combining these results, they revealed several key features of lithosphere and asthenosphere structure. A rapid change from thin (~70–80 km) lithosphere in the western United States (WUS) to thick lithosphere (~200 km) in the central, cratonic part of the continent closely follows the Rocky Mountain Front. Changes with depth of the fast axis direction of azimuthal anisotropy reveal the presence of two layers in the cratonic lithosphere, corresponding to the fast-to-slow discontinuity found in receiver functions. Below the lithosphere, azimuthal anisotropy manifests a maximum, stronger in the WUS than under the craton, and the fast axis of anisotropy aligns with the absolute plate motion. In the WUS, this zone is confined between 70 and 150 km depths, decreasing in strength with depth from the top, from the Rocky Mountain Front to the San Andreas Fault system and the Juan de Fuca/Gorda ridges. This result suggests that shear associated with lithosphere–asthenosphere coupling dominates mantle deformation down to this depth in the western part of the continent. Radial anisotropy results show that Vsh > Vsv under the continent and its borders down to ~200 km depth, with stronger radial anisotropy in the bordering oceanic regions. Across the continent and below 200 km depth, alternating zones of weaker and stronger radial anisotropy, with predominantly Vsh < Vsv, correlate with zones of small lateral changes in the fast axis direction of anisotropy, and > average Vs below the lithosphere, suggesting the presence of small-scale convection with a wavelength of ~2000 km. In the WUS, complex 3-D patterns of isotropic velocity and anisotropy reflect mantle dynamics associated with the rich tectonic history of the region (Yuan et al., 2011).

5. Discussion and conclusions

One problem of anisotropy tomography is that there could be a trade-off between velocity heterogeneity and anisotropy, in particular when the ray path coverage is insufficient in different directions. However, recent studies show that the trade-off problem can be resolved when earthquakes and seismic stations used in a tomographic inversion are densely and uniformly distributed in the study area (e.g., Wang and Zhao, 2012, 2013). Huang et al. (2015) made comprehensive tests with synthetic data to investigate the robustness of P-wave anisotropic tomography, especially the trade-off between the isotropic and anisotropic velocity structures. Their results show that, for P-wave azimuthal anisotropy, good azimuthal coverage of rays is necessary to obtain a stable tomographic result. They plotted the ray-azimuth ellipse at each grid node to represent the azimuthal coverage and proposed to use the normalized length of the short-axis (NLS) of the ellipse for examining the reliability of P-wave anisotropic tomography. The isotropic and anisotropic structures are strongly coupled with each other (including the smearing, strengthening and weakening effects) when the rays used are distributed in a narrow azimuthal range (e.g., when the azimuthal range is <30° and NLS is <0.2). The degree of trade-off can be reduced with better azimuthal coverage, when the ray azimuthal range is ~60° and NLS is ~0.2–0.3. The trade-off becomes very small when the azimuthal coverage reaches 90° (NLS = 0.3–0.5). The isotropic and anisotropic structures could be restored independently without smearing when the azimuthal coverage exceeds 120° (NLS >0.5).

In Vp radial anisotropy tomography, the isotropic and anisotropic structures are also strongly coupled when data of only the horizontal or vertical rays are used in the tomographic inversion (Huang et al., 2015). The tomographic results can be improved significantly when both local shallow and deep earthquake are used in the inversion. An NLS (estimated from the ray-incidence ellipses representing the incidence coverage) of ~0.2 could yield reliable isotropic and anisotropic structures with little smearing effect. For obtaining a reliable tomography of isotropic and anisotropic structures, it is necessary to use local and teleseismic data simultaneously, whereas the teleseismic data alone are not sufficient (Huang et al., 2015).

Yoshizawa et al. (2010) determined a 3-D Vs tomography of the upper mantle down to ~200 km depth beneath the Japan Islands and the surrounding regions using measurements of inter-station phase velocities of the fundamental-mode Rayleigh and Love waves (Fig. 14). Their isotropic Vs tomography shows the high-V subducting Pacific and PHS slabs and low-V anomalies in the mantle wedge above the slabs (Fig. 14a,b). They also simultaneously inverted the phase-velocity maps of Rayleigh and Love waves in the period range of 30 to 80 s to construct a 3-D radial anisotropic Vs model. Their model shows a remarkable radial anisotropy with Vsh > Vsv in the mantle wedge beneath Tohoku and Kyushu, whereas only weak anisotropy is revealed beneath the Japan Sea (Fig. 14c). This radial anisotropy result revealed by surface-wave tomography (Yoshizawa et al., 2010) is quite different from that of P-wave anisotropic tomography (Wang and Zhao, 2013; Huang et al., 2015) which shows Vpv > Vph existing in the low-V zones in the mantle wedge (Fig. 3).

The discrepancy in the mantle-wedge radial anisotropy between the surface-wave and body-wave models is a puzzle, but also an intriguing topic for future studies. There are several possibilities which may cause such a discrepancy. The first is the different resolution scales of the surface-wave and body-wave tomographic models. The body-wave models have a much higher resolution, and they show spatial variations in the radial anisotropy in the mantle wedge, i.e., Vpv > Vph in the low-V zones, whereas Vpv < Vph in the high-V and average-velocity parts in the mantle wedge (Fig. 3). In contrast, the surface-wave model shows a uniform radial anisotropy with Vsh > Vsv in the entire mantle wedge beneath Tohoku and Kyushu (Fig. 14c). The second possibility is the trade-off between the structures of the mantle wedge and the subducting slab. The body-wave model could distinguish the slab and the mantle wedge, because the precise location of the slab boundary is taken into account in the tomographic inversion (Zhao et al., 1992, 2012; Wang and Zhao, 2013; Huang et al., 2015). However, a trade-off could occur for the radial anisotropy structure between the slab and the mantle wedge, because the ray distribution of P-wave data from the intermediate-depth earthquakes in the slab may not be good enough for resolving the radial anisotropy within the slab. Note that the body-wave models show Vpv < Vph in the Pacific and PHS slabs (Wang and Zhao, 2013). A similar trade-off between the slab and the mantle wedge could also occur in the surface-wave tomography because of its limited vertical resolution, e.g., the high-V slab anomaly extends to the overlying mantle wedge (see the vertical cross-sections in Fig. 14a,b). The third possibility is that P-wave anisotropy may not be identical to the shear-wave anisotropy for the mantle minerals under the complex conditions of temperature, pressure, stress regime, and in the presence of water, melts, and lithological variations (e.g., Karato et al., 2008).

This puzzle may be resolved by improving the resolution and quality of both the body-wave and surface-wave tomography models, and by better understanding the nature of P and S wave anisotropy through mineral physics studies.

A thorough understanding of seismic anisotropy and heterogeneity in the Earth's interior can be achieved by combining various seismological information, such as body-wave and surface-wave data, shear-wave splitting measurements, and receiver functions, all of which require dense and high-quality seismic networks covering land as well as oceanic regions. A wealth of information from other branches of geosciences is also necessary for better interpreting the seismological observations.

Acknowledgements

We thank Prof. Y. Eyuboglu and Prof. M. Santosh (guest editors) for inviting us to submit this paper to the GR special issue *Convergent Margins and Related Processes*. We are grateful to Jian Wang, You Tian, Zhouchuan Huang, Wei Wei, Lucy Liu and Bin Cheng for efficient research collaborations and thoughtful discussions on seismic anisotropy

tomography. This work was partially supported by research grants from the Japan Society for the Promotion of Science (Kiban-S 11050123) and MEXT (26106005) to D. Zhao. Two anonymous referees provided thoughtful review comments and suggestions which have improved this paper.

References

Abdelwahed, M., Zhao, D., 2005. Waveform modelling of local earthquakes in southwest Japan. Earth, Planets and Space 57, 1039–1054.

Abdelwahed, M., Zhao, D., 2007. Deep structure of the Japan subduction zone. Physics of the Earth and Planetary Interiors 162, 32–52.

Abdelwahed, M., Zhao, D., 2014. Genetic waveform modeling for the crustal structure in Northeast Japan. Journal of Asian Earth Sciences 89, 66–75.

Abt, D., Fischer, K., 2008. Resolving three-dimensional anisotropic structure with shear wave splitting tomography. Geophysical Journal International 173, 859–886.

Abt, D., Fischer, K., Abers, G., et al., 2009. Shear wave anisotropy beneath Nicaragua and Costa Rica: Implications for flow in the mantle wedge. Geochemistry, Geophysics, Geosystems 10, Q05S15.

Anderson, D.L., 1989. Theory of the Earth. Blackwell Science Publication 366.

Ando, M., Ishikawa, Y., Yamasaki, F., 1983. Shear wave polarization anisotropy in the upper mantle beneath Honshu. Journal of Geophysical Research 88, 5850–5864.

Audoine, E., Savage, M., Gledhill, K., 2000. Seismic anisotropy from local earthquakes in the transition region from a subduction to a strike-slip plate boundary, New Zealand. Journal of Geophysical Research 105, 8013–8033.

Audoine, E., Savage, M., Gledhill, K., 2004. Anisotropic structure under a back arc spreading region, the Taupo Volcanic Zone, New Zealand. Journal of Geophysical Research 109, B11305.

Babuska, V., Cara, M., 1991. Seismic Anisotropy in the Earth. Kluwer Academy Publishers, Dordrecht (217 pp.).

Babuska, V., Plomerova, J., Sileny, J., 1984. Spatial variations of P residuals and deep structure of the European lithospere. Geophysical Journal of the Royal Astronomical Society 79, 363–383.

Backus, G., 1965. Possible forms of seismic anisotropy of uppermost mantle under oceans. Journal of Geophysical Research 70, 3429–3439.

Barclay, A., Toomey, D., Solomon, S., 1998. Seismic structure and crustal magmatism at the Mid-Atlantic Ridge, 35 degrees N. Journal of Geophysical Research 103, 17827–17844.

Becker, T., 2012. On recent seismic tomography for the western United States. Geochemistry, Geophysics, Geosystems 13, Q01W10.

Bokelmann, G., 1995. P-wave array polarization analysis and effective anisotropy of the brittle crust. Geophysical Journal International 120, 145–162.

Bokelmann, G., 2002. Convection-driven motion of the North American craton: Evidence from P-wave anisotropy. Geophysical Journal International 148, 278–287.

Cara, M., 2002. Seismic anisotropy. In: Lee, W.H.K., Kanamori, H., Jennings, P.C., Kisslinger, C. (Eds.), International Handbook of Earthquake and Engineering Seismology, pp. 875–885.

Carr, M., Saginor, I., Alvarado, G., et al., 2007. Element fluxes from the volcanic front of Nicaragua and Costa Rica. Geochemistry, Geophysics, Geosystems 8, Q06001.

Chen, C., Zhao, D., Wu, S., 2014. Crust and upper mantle structure of New Madrid Seismic Zone: Insight into intraplate earthquakes. Physics of the Earth and Planetary Interiors 230, 1–14.

Chen, C., Zhao, D., Wu, S., 2015. Tomographic imaging of the Cascadia subduction zone: Constraints on the Juan de Fuca slab. Tectonophysics 647, 73–88.

Cheng, B., Zhao, D., Zhang, G., 2011. Seismic tomography and anisotropy in the source area of the 2008 Iwate-Miyagi earthquake (M7.2). Physics of the Earth and Planetary Interiors 184, 172–185.

Cheng, B., Cheng, S., Zhang, G., Zhao, D., 2014. Seismic structure of the Helan-Liupan-Ordos western margin tectonic belt in North-Central China and its geodynamic implications. Journal of Asian Earth Sciences 87, 141–156.

Christensen, N.I., 1984. The magnitude, symmetry and origin of upper mantle anisotropy based on fabric analyses of ultramafic tectonites. Geophysical Journal of the Royal Astronomical Society 76, 89–111.

Christensen, D., Abers, G., 2010. Seismic anisotropy under central Alaska from SKS splitting observations. Journal of Geophysical Research 115, B04315.

Crampin, S., 1984. Effective anisotropic constants for wave-propagation through cracked solids. Geophysical Journal of the Royal Astronomical Society 76, 135–145.

Eberhart-Phillips, D., Henderson, C., 2004. Including anisotropy in 3-D velocity inversion and application to Marlborough, New Zealand. Geophysical Journal International 156, 237–254.

Eberhart-Phillips, D., Reyners, M., 2009. Three-dimensional distribution of seismic anisotropy in the Hikurangi subduction zone beneath the central North Island, New Zealand. Journal of Geophysical Research 114, B06301.

Eberhart-Phillips, D., Reyners, M., Faccenda, M., Naliboff, J., 2013. Along-strike variation in subducting plate seismicity and mantle wedge attenuation related to fluid release beneath the North Island, New Zealand. Physics of the Earth and Planetary Interiors 225, 12–27.

Eken, T., Plomerova, J., Roberts, R., Vecsey, L., Babuska, V., 2010. Seismic anisotropy of the mantle lithosphere beneath the Swedish National Seismological Network (SNSN). Tectonophysics 480, 241–258.

Engdahl, E., Lee, W., 1976. Relocation of local earthquakes by seismic ray tracing. Journal of Geophysical Research 81, 4400–4406.

Fichtner, A., Kennett, B., Igel, H., Bunge, H., 2010. Full waveform tomography for radially anisotropic structure: new insights into present and past states of the Australasian upper mantle. Earth and Planetary Science Letters 290, 270–280.

Fouch, M., Rondenay, S., 2006. Seismic anisotropy beneath stable continental interiors. Physics of the Earth and Planetary Interiors 158, 292–320.

Gardner, T., Verdonck, D., Pinter, N., 1992. Quaternary uplift astride the aseismic Cocos Ridge, Pacific coast, Costa Rica. Geological Society of America Bulletin 104, 219–232.

Gresillaud, A., Cara, M., 1996. Anisotropy and P-wave tomography: a new approach for inverting teleseismic data from a dense array of stations. Geophysical Journal International 126, 77–91.

Hammond, J., Wookey, J., Kaneshima, S., Inoue, H., Yamashina, T., Harjadi, P., 2010. Systematic variation in anisotropy beneath the mantle wedge in the Java-Sumatra subduction system from shear-wave splitting. Physics of the Earth and Planetary Interiors 178, 189–201.

Hasemi, A., Ishii, H., Takagi, A., 1984. Fine structure beneath the Tohoku District, northeastern Japan arc, as derived by an inversion of P-wave arrival times from local earthquakes. Tectonophysics 101, 245–265.

He, R., Zhao, D., Gao, R., Zheng, H., 2010. Tracing the Indian lithospheric mantle beneath central Tibetan Plateau using teleseismic tomography. Tectonophysics 491, 230–243.

Hearn, T., 1984. Pn travel times in Southern California. Journal of Geophysical Research 89, 1843–1855.

Hearn, T., 1996. Anisotropic Pn tomography in the western United States. Journal of Geophysical Research 101, 8403–8414.

Hess, H., 1964. Seismic anisotropy of uppermost mantle under oceans. Nature 203, 629–631.

Hirahara, K., 1988. Detection of three-dimensional velocity anisotropy. Physics of the Earth and Planetary Interiors 51, 71–85.

Hirahara, K., Ishikawa, Y., 1984. Travel-time inversion for three-dimensional P-wave velocity anisotropy. Journal of Physics of the Earth 32, 197–218.

Hiramatsu, Y., Ando, M., Ishikawa, Y., 1997. ScS wave splitting of deep earthquakes around Japan. Geophysical Journal International 128, 409–424.

Huang, Z., Zhao, D., 2013. Mapping P-wave azimuthal anisotropy in the crust and upper mantle beneath the United States. Physics of the Earth and Planetary Interiors 225, 28–40.

Huang, Z., Zhao, D., Wang, L., 2011a. Shear-wave anisotropy in the crust, mantle wedge and the subducting Pacific slab under Northeast Japan. Geochemistry, Geophysics, Geosystems 12, Q01002.

Huang, Z., Zhao, D., Wang, L., 2011b. Frequency-dependent shear-wave splitting and multilayer anisotropy in Northeast Japan. Geophysical Research Letters 38, L08302.

Huang, Z., Zhao, D., Wang, L., 2011c. Seismic heterogeneity and anisotropy of the Honshu arc from the Japan Trench to the Japan Sea. Geophysical Journal International 184, 1428–1444.

Huang, Z., Zhao, D., Hasegawa, A., Umino, N., Park, J., Kang, I., 2013. Aseismic deep subduction of the Philippine Sea plate and slab window. Journal of Asian Earth Sciences 75, 82–94.

Huang, Z., Wang, P., Zhao, D., Wang, L., Xu, M., 2014. Three-dimensional P-wave azimuthal anisotropy in the lithosphere beneath China. Journal of Geophysical Research 119, 5686–5712.

Huang, Z., Zhao, D., Liu, X., 2015. On the trade-off between seismic anisotropy and heterogeneity: Numerical simulations and application to Northeast Japan. Journal of Geophysical Research 120, 3255–3277.

Ishise, M., Oda, H., 2005. Three-dimensional structure of P-wave anisotropy beneath the Tohoku district, northeast Japan. Journal of Geophysical Research 110, B07304.

Ishise, M., Oda, H., 2008. Subduction of the Philippine Sea slab in view of P-wave anisotropy. Physics of the Earth and Planetary Interiors 166, 83–96.

Ishise, M., Kawakatsu, K., Shiomi, K., 2012. Anisotropic velocity structure under the Japan Islands using Hi-net arrival-time data. (1) Reexamination of the 3-D anisotropic velocity structure beneath Northeast Japan. Program and Abstracts of the Annual Meeting of Seismological Society of Japan, Hakodate, Japan, p. B12-02.

Jung, H., Karato, S., 2001. Water-induced fabric transitions in olivine. Science 293, 1460–1463.

Kaneshima, S., 1990. Origin of crustal anisotropy: Shear wave splitting studies in Japan. Journal of Geophysical Research 95, 1111–1133.

Karato, S., Wu, P., 1993. Rheology of the upper mantle: A synthesis. Science 260, 771–778.

Karato, S., Jung, H., Katayama, I., Skemer, P., 2008. Geodynamic significance of seismic anisotropy of the upper mantle: new insights from laboratory studies. Annual Review of Earth and Planetary Sciences 36, 59–95.

Klosko, E., Wu, F., Anderson, H., Eberhart-Phillips, D., McEvilly, T., Audoine, E., Savage, M., Gledhill, K., 1999. Upper mantle anisotropy in the New Zealand region. Geophysical Research Letters 26, 1497–1500.

Koulakov, I., Jakovlev, A., Luehr, B., 2009. Anisotropic structure beneath central Java from local earthquake tomography. Geochemistry, Geophysics, Geosystems 10, Q02011.

Koulakov, I., Kukarina, E., Fathi, I., Khrepy, S., Al-Arifi, N., 2015. Anisotropic tomography of Hokkaido reveals delamination-induced flow above a subducting slab. Journal of Geophysical Research 120, 3219–3239.

Lees, J., Wu, H., 1999. P wave anisotropy, stress, and crack distribution at Coso geothermal field, California. Journal of Geophysical Research 104, 17955–17973.

Lei, J., Zhao, D., 2005. P-wave tomography and origin of the Changbai intraplate volcano in Northeast Asia. Tectonophysics 397, 281–295.

Lei, J., Zhao, D., 2009. Structural heterogeneity of the Longmenshan fault zone and the mechanism of the 2008 Wenchuan earthquake (Ms 8.0). Geochemistry, Geophysics, Geosystems 10, Q10010.

Li, Z., Zhang, H., Peng, Z., 2014. Structure-controlled seismic anisotropy along the Karadere–Düzce branch of the North Anatolian Fault revealed by shear-wave splitting tomography. Earth and Planetary Science Letters 391, 319–326.

Lin, Y., Zhao, L., Hung, S., 2014. Full-wave multiscale anisotropy tomography in Southern California. Geophysical Research Letters 41, 8809–8817.
Liu, X., Zhao, D., 2014. Structural control on the nucleation of megathrust earthquakes in the Nankai subduction zone. Geophysical Research Letters 41, 8288–8293.
Liu, X., Zhao, D., 2015. Seismic attenuation tomography of the Southwest Japan arc: New insight into subduction dynamics. Geophysical Journal International 201, 135–156.
Liu, X., Zhao, D., Li, S., 2013. Seismic heterogeneity and anisotropy of the southern Kuril arc: Insight into megathrust earthquakes. Geophysical Journal International 194, 1069–1090.
Liu, X., Zhao, D., Li, S., 2014. Seismic attenuation tomography of the Northeast Japan arc: Insight into the 2011 Tohoku earthquake (Mw 9.0) and subduction dynamics. Journal of Geophysical Research 119, 1094–1118.
Long, M., 2013. Constraints on subduction geodynamics from seismic anisotropy. Reviews of Geophysics 51, 76–112.
Maupin, V., Park, J., 2007. Theory and observations – wave propagation in anisotropic media. In: Schubert, G. (Ed.), Treatise on geophysics. Elsevier, Amsterdam, pp. 289–321.
Menke, W., 2015. Equivalent heterogeneity analysis as a tool for understanding the resolving power of anisotropic travel-time tomography. Bulletin of the Seismological Society of America 105, 719–733.
Mishra, O.P., Zhao, D., 2003. Crack density, saturation rate and porosity at the 2001 Bhuj, India, earthquake hypocenter: A fluid driven earthquake? Earth and Planetary Science Letters 212, 393–405.
Mishra, O.P., Zhao, D., Umino, N., Hasegawa, A., 2003. Tomography of northeast Japan forearc and its implications for interplate seismic coupling. Geophysical Research Letters 30, GL017736.
Mochizuki, E., 1995. Anisotropic tomography of P-wave traveltimes. Geophysical Journal International 123, 297–300.
Mochizuki, E., 1997. Nonuniqueness of two-dimensional anisotropic tomography. Bulletin of the Seismological Society of America 87, 261–264.
Montagner, J., 2011. Earth's structure: global. In: Gupta, H. (Ed.), Encyclopedia of Solid Earth Geophysics. Springer, Netherlands, pp. 144–154.
Montagner, J., Tanimoto, T., 1991. Global upper mantle tomography of seismic velocities and anisotropies. Journal of Geophysical Research 96, 20337–20351.
Monteiller, V., Chevrot, S., 2011. High-resolution imaging of the deep anisotropic structure of the San Andreas Fault system beneath southern California. Geophysical Journal International 186, 418–446.
Nakajima, J., Shimizu, J., Hori, S., Hasegawa, A., 2006. Shear-wave splitting beneath the southwestern Kurile arc and northeastern Japan arc: a new insight into mantle return flow. Geophysical Research Letters 33. http://dx.doi.org/10.1029/2005GL025053.
Nettles, M., Dziewonski, A., 2008. Radially anisotropic shear velocity structure of the upper mantle globally and beneath North America. Journal of Geophysical Research 113, B02303.
Nishimura, C., Forsyth, D., 1988. Rayleigh wave phase velocities in the Pacific with implications for azimuthal anisotropy and lateral heterogeneities. Geophysical Journal International 94, 479–501.
Okada, T., Matsuzawa, T., Hasegawa, A., 1995. Shear-wave polarization anisotropy beneath the north-eastern part of Honshu, Japan. Geophysical Journal International 123, 781–797.
Padhy, S., Mishra, O.P., Zhao, D., Wei, W., 2011. Crustal heterogeneity in the 2007 Noto-Hanto earthquake area and its geodynamical implications. Tectonophysics 509, 55–68.
Park, J., Yu, Y., 1993. Seismic determination of elastic anisotropy and mantle flow. Science 261, 1159–1162.
Plomerova, J., Sileny, J., Babuska, V., 1996. Joint interpretation of upper-mantle anisotropy based on teleseismic P-travel time delays and inversion of shear-wave splitting parameters. Physics of the Earth and Planetary Interiors 95, 293–309.
Plomerova, J., Vecsey, L., Babuska, V., 2011. Domains of Archean mantle lithosphere deciphered by seismic anisotropy - Inferences from the LAPNET array in northern Fennoscandia. Solid Earth 2, 303–313.
Qi, C., Zhao, D., Chen, Y., 2007. Search for deep slab segments under Alaska. Physics of the Earth and Planetary Interiors 165, 68–82.
Rabbel, W., Koulakov, I., Dinc, A., Jakovlev, A., 2011. Arc-parallel shear deformation and escape flow in the mantle wedge of the Central America subduction zone: evidence from P wave anisotropy. Geochemistry, Geophysics, Geosystems 12, Q05S31.
Raitt, R., Shor, G., Francis, T., Morris, G., 1969. Anisotropy of Pacific upper mantle. Journal of Geophysical Research 74, 3095–3109.
Reyners, M., 2013. The central role of the Hikurangi Plateau in the Cenozoic tectonics of New Zealand and the Southwest Pacific. Earth and Planetary Science Letters 361, 460–468.
Ritzwoller, M., Lavely, E., 1995. Three-dimensional seismic models of the Earth's mantle. Reviews of Geophysics 33, 1–66.
Salah, M., Seno, T., Iidaka, T., 2008. Upper mantle anisotropy beneath central and southwest Japan: An insight into subduction-induced mantle flow. Journal of Geodynamics 46, 21–37.
Savage, M.K., 1999. Seismic anisotropy and mantle deformation: what have we learned from shear wave splitting? Reviews of Geophysics 37, 65–106.
Shi, Y., Gao, Y., Wu, J., Luo, Y., Su, Y., 2006. Seismic anisotropy of the crust in Yunnan, China: polarizations of fast shear-waves. Acta Seismologica Sinica 19, 620–632.
Silver, P.G., 1996. Seismic anisotropy beneath the continents: Probing the depths of geology. Annual Review of Earth and Planetary Sciences 24, 385–432.
Sun, A., Zhao, D., Ikeda, M., Chen, Y., Chen, Q., 2008. Seismic imaging of southwest Japan using P and PmP data: Implications for arc magmatism and seismotectonics. Gondwana Research 14, 535–542.
Tanimoto, T., Anderson, D., 1984. Mapping convection in the mantle. Geophysical Research Letters 11, 327–336.
Terada, T., Hiramatsu, Y., Mizukami, T., 2013. Shear wave anisotropy beneath the volcanic front in South Kyushu area, Japan: Development of C-type olivine CPO under H2O-rich conditions. Journal of Geophysical Research 118, 4253–4264.
Tian, Y., Zhao, D., 2012a. Seismic anisotropy and heterogeneity in the Alaska subduction zone. Geophysical Journal International 190, 629–649.
Tian, Y., Zhao, D., 2012b. P-wave tomography of the Western United States: Insight into the Yellowstone hotspot and the Juan de Fuca slab. Physics of the Earth and Planetary Interiors 200, 72–84.
Tian, Y., Zhao, D., 2013. Reactivation and mantle dynamics of North China Craton: Insight from P-wave anisotropy tomography. Geophysical Journal International 195, 1796–1810.
Tong, P., Zhao, D., Yang, D., 2011. Tomography of the 1995 Kobe earthquake area: Comparison of finite-frequency and ray approaches. Geophysical Journal International 187, 278–302.
Tong, P., Zhao, D., Yang, D., 2012. Tomography of the 2011 Iwaki earthquake (M 7.0) and Fukushima nuclear power plant area. Solid Earth 3, 43–51.
Tsumura, N., Matsumoto, S., Horiuchi, S., Hasegawa, A., 2000. Three-dimensional attenuation structure beneath the northeastern Japan arc estimated from spectra of small earthquakes. Tectonophysics 319, 241–260.
Umino, N., Hasegawa, A., 1984. Three-dimensional Qs structure in the northeastern Japan arc. Journal of Seismological Society of Japan 37, 217–228.
Umino, N., Hasegawa, A., Matsuzawa, T., 1995. sP depth phase at small epicentral distances and estimated subducting plate boundary. Geophysical Journal International 120, 356–366.
von Huene, R., Hoffmann, J., Holler, P., Leon, R., et al., 1995. Morphotectonics of the Pacific convergent margin of Costa Rica. Special Papers of the Geological Society of America 295, 291–307.
Wang, Y., Tape, C., 2014. Seismic velocity structure and anisotropy of the Alaska subduction zone based on surface wave tomography. Journal of Geophysical Research 119, 8845–8865.
Wang, Z., Zhao, D., 2006. Seismic images of the source area of the 2004 Mid-Niigata prefecture earthquake in Northeast Japan. Earth and Planetary Science Letters 244, 16–31.
Wang, J., Zhao, D., 2008. P-wave anisotropic tomography beneath Northeast Japan. Physics of the Earth and Planetary Interiors 170, 115–133.
Wang, J., Zhao, D., 2009. P-wave anisotropic tomography of the crust and upper mantle under Hokkaido, Japan. Tectonophysics 469, 137–149.
Wang, J., Zhao, D., 2010. Mapping P-wave anisotropy of the Honshu arc from Japan Trench to the back-arc. Journal of Asian Earth Sciences 39, 396–407.
Wang, J., Zhao, D., 2012. P wave anisotropic tomography of the Nankai subduction zone in Southwest Japan. Geochemistry, Geophysics, Geosystems 13, Q05017.
Wang, J., Zhao, D., 2013. P-wave tomography for 3-D radial and azimuthal anisotropy of Tohoku and Kyushu subduction zones. Geophysical Journal International 193, 1166–1181.
Wang, Z., Zhao, D., Wang, J., 2010. Deep structure and seismogenesis of the north-south seismic zone in Southwest China. Journal of Geophysical Research 115, B12334.
Wang, J., Zhao, D., Yao, Z., 2013. Crustal and uppermost mantle structure and seismotectonics of North China Craton. Tectonophysics 582, 177–187.
Wang, J., Wu, H., Zhao, D., 2014. P wave radial anisotropy tomography of the upper mantle beneath the North China Craton. Geochemistry, Geophysics, Geosystems 15, 2195–2210.
Watanabe, M., Oda, H., 2014. Regional variations of the shear-wave polarization anisotropy in the crust and mantle wedge beneath the Tohoku district. Physics of the Earth and Planetary Interiors 235, 49–65.
Wei, W., Xu, J., Zhao, D., Shi, Y., 2012. East Asia mantle tomography: New insight into plate subduction and intraplate volcanism. Journal of Asian Earth Sciences 60, 88–103.
Wei, W., Zhao, D., Xu, J., 2013. P-wave anisotropic tomography in Southeast Tibet: New insight into the lower crustal flow and seismotectonics. Physics of the Earth and Planetary Interiors 222, 47–57.
Wei, W., Zhao, D., Xu, J., Wei, F., Liu, G., 2015. P and S wave tomography and anisotropy in Northwest Pacific and East Asia: Constraints on stagnant slab and intraplate volcanism. Journal of Geophysical Research 120, 1642–1666.
Wu, H., Lees, J., 1999. Cartesian parameterization of anisotropic traveltime tomography. Geophysical Journal International 137, 64–80.
Wustefeld, A., Bokelmann, G., Barruol, G., Montagner, J., 2009. Identifying global seismic anisotropy patterns by correlating shear-wave splitting and surface wave data. Physics of the Earth and Planetary Interiors 176, 198–212.
Xia, S., Zhao, D., Qiu, X., 2008. The 2007 Niigata earthquake: Effect of arc magma and fluids. Physics of the Earth and Planetary Interiors 166, 153–166.
Yoshizawa, K., Miyake, K., Yomogida, K., 2010. 3D upper mantle structure beneath Japan and its surrounding region from inter-station dispersion measurements of surface waves. Physics of the Earth and Planetary Interiors 183, 4–19.
Yuan, H., Romanowicz, B., Fischer, K., Abt, D., 2011. 3-D shear wave radially and azimuthally anisotropic velocity model of the North American upper mantle. Geophysical Journal International 184, 1237–1260.
Zhang, Z., Schwartz, S., 1994. Seismic anisotropy in the shallow crust of the Loma Prieta segment of the San Andreas fault system. Journal of Geophysical Research 99, 9651–9661.
Zhang, H.J., Liu, Y., Thurber, C., Roecker, S., 2007. Three-dimensional shear-wave splitting tomography in the Parkfield, California, region. Geophysical Research Letters 34, L24308.
Zhang, H., Zhao, D., Zhao, J., Xu, Q., 2012. Convergence of the Indian and Eurasian plates under eastern Tibet revealed by seismic tomography. Geochemistry, Geophysics, Geosystems 13, Q06W14.
Zhao, D., 2012. Tomography and dynamics of Western-Pacific subduction zones. Monographs on Environment, Earth and Planets 1, 1–70.
Zhao, D., 2015a. Multiscale seismic tomography. Springer (304 pp.).

Zhao, D., 2015b. The 2011 Tohoku earthquake (Mw 9.0) sequence and subduction dynamics in Western Pacific and East Asia. Journal of Asian Earth Sciences 98, 26–49.
Zhao, D., Tian, Y., 2013. Changbai intraplate volcanism and deep earthquakes in East Asia: A possible link? Geophysical Journal International 195, 706–724.
Zhao, D., Hasegawa, A., Horiuchi, S., 1992. Tomographic imaging of P and S wave velocity structure beneath northeastern Japan. Journal of Geophysical Research 97, 19909–19928.
Zhao, D., Hasegawa, A., Kanamori, H., 1994. Deep structure of Japan subduction zone as derived from local, regional and teleseismic events. Journal of Geophysical Research 99, 22313–22329.
Zhao, D., Christensen, D., Pulpan, H., 1995. Tomographic imaging of the Alaska subduction zone. Journal of Geophysical Research 100, 6487–6504.
Zhao, D., Lei, J., Tang, Y., 2004. Origin of the Changbai volcano in northeast China: Evidence from seismic tomography. Chinese Science Bulletin 49, 1401–1408.
Zhao, D., Maruyama, S., Omori, S., 2007. Mantle dynamics of western Pacific to East Asia: New insight from seismic tomography and mineral physics. Gondwana Research 11, 120–131.
Zhao, D., Santosh, M., Yamada, A., 2010. Dissecting large earthquakes in Japan: Role of arc magma and fluids. Island Arc 19, 4–16.
Zhao, D., Huang, Z., Umino, N., Hasegawa, A., Yoshida, T., 2011a. Seismic imaging of the Amur-Okhotsk plate boundary zone in the Japan Sea. Physics of the Earth and Planetary Interiors 188, 82–95.
Zhao, D., Huang, Z., Umino, N., Hasegawa, A., Kanamori, H., 2011b. Structural heterogeneity in the megathrust zone and mechanism of the 2011 Tohoku-oki earthquake (Mw 9.0). Geophysical Research Letters 38, L17308.
Zhao, D., Wei, W., Nishizono, Y., Inakura, H., 2011c. Low-frequency earthquakes and tomography in western Japan: Insight into fluid and magmatic activity. Journal of Asian Earth Sciences 42, 1381–1393.
Zhao, D., Yanada, T., Hasegawa, A., Umino, N., Wei, W., 2012. Imaging the subducting slabs and mantle upwelling under the Japan Islands. Geophysical Journal International 190, 816–828.
Zhao, D., Kitagawa, H., Toyokuni, G., 2015. A water wall in the Tohoku forearc causing large crustal earthquakes. Geophysical Journal International 200, 149–172.

Dapeng Zhao is a professor at the Department of Geophysics, Tohoku University, Sendai, Japan. He received his B.Sc. (1984) from Peking University, and his M.Sc. (1988) and Ph.D. (1991) from Tohoku University. He was a postdoctoral fellow at the California Institute of Technology during 1992–1995, and associate professor during 1998–2002 and professor during 2003–2007 at Ehime University. In April 2007 he moved to Tohoku University as a professor. His research interests include earthquake seismology, seismic tomography, Earth structure and dynamics from local to global scales, subduction zones, hotspots, mantle plumes, moonquakes and lunar interior structure. He has published more than 200 research papers with his coworkers on these topics in refereed international journals, which have been cited over 9000 times (H-index = 50). He has been awarded the 2014 Island Arc Award by the Geological Society of Japan. To date, Prof. D. Zhao has advised more than 40 graduate students and postdoctoral researchers. Now he is an editor of the *Journal of Asian Earth Sciences*.

Sheng Yu is a professor of geophysics at National Natural Science Foundation of China (NSFC), received his B.Sc. (1986) from Dalian University of Technology, China, M.Sc. (1991) from Institute of Geophysics, Chinese Academy of Sciences (CAS) and Ph.D. (2000) from Institute of Geology and Geophysics, CAS. He had been a visiting scholar at University of Manitoba, Canada from 1991 to 1992. He joined the CAS Institute of Geophysics in 1986, and became an associate professor in 1994. In May 1995 he moved to NSFC and became the head of the Division of Geophysics and Space Physics. He became a full professor of geophysics in 2004. His research interests include magnetotellurics, seismic tomography, geodesy and geodynamics.

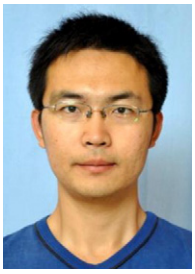

Xin Liu obtained his B.Sc. (2007) from China University of Geosciences (Beijing), and his M.Sc. (2010) and Ph.D. (2013) from Ocean University of China. Now he is a postdoctoral fellow at the Department of Geophysics, Tohoku University, Sendai, Japan. His research interests include seismic tomography, structural geology and tectonics.